Dynamic fault interaction during a fluid-injection induced earthquake: The 2017 Mw 5.5 Pohang event

Kadek Hendrawan Palgunadi[1*], Alice-Agnes Gabriel[2], Thomas Ulrich[2], José Ángel Lopéz-Comino[3i], Paul Martin Mai[1]

1. Physical Science and Engineering, King Abdullah University of Science and Technology, Thuwal, Saudi Arabia
2. Department of Earth and Environmental Sciences, Geophysics, Ludwig-Maximilians-Universität München, Theresienstr. 41, 80333 Munich, Germany
3. Institute of Geosciences University of Potsdam, Potsdam-Golm, Germany.

***corresponding author: kadek.palgunadi@kaust.edu.sa**

Abstract:

The November 15^{th}, 2017 Mw 5.5 Pohang earthquake (South Korea) has been linked to hydraulic stimulation and fluid injections, making this the largest induced seismic event associated with an Enhanced Geothermal System (EGS). To understand its source dynamics and fault interactions, we conduct the first 3D high-resolution spontaneous dynamic rupture simulations of an induced earthquake. We account for topography, off-fault plastic deformation under depth-dependent bulk cohesion, rapid velocity weakening friction and 1D subsurface structure. A guided fault reconstruction approach that clusters spatio-temporal aftershock locations (including their uncertainties) is used to identify a main and a secondary fault plane which intersect under a shallow angle of 15°. Based on simple Mohr-Coulomb failure analysis and 180 dynamic rupture experiments in which we vary local stress loading conditions, fluid pressure, and relative fault strength, we identify preferred two fault plane scenarios that well reproduce observations. We find that the regional far-field tectonic stress regime promotes pure strike-slip faulting, while local

[i]also at Instituto Andaluz de Geofísica, Universidad de Granada, Spain; Departamento de Física Teórica y del Cosmos, Universidad de Granada, Spain; Physical Science and Engineering, King Abdullah University of Science and Technology, Thuwal, Saudi Arabia

stress conditions constrained by borehole logging generate the observed thrust faulting component. Our preferred model is characterized by overpressurized pore fluids, non-optimally oriented but dynamically weak faults and a close to critical local stress state. In our model, earthquake rupture "jumps" to the secondary fault by dynamic triggering, generating a measurable non-double couple component. Our simulations suggest that complex dynamic fault interaction may occur during fluid-injection induced earthquakes and that local stress perturbations dominate over the regional stress conditions. These findings, therefore, have important implications for seismic hazard in active geo-reservoir.

1. Introduction

The Korean Peninsula is known to have a rather low-level of seismicity (compared to neighboring countries like China and Japan) because it lies on the continental margin of the east Eurasian plate. However, on November 15^{th}, 2017 (05:29:31 UTC), a magnitude Mw 5.5 earthquake occurred (hereinafter the Pohang earthquake), the second-largest recorded earthquake in South Korea following the 2016 Mw 5.5 Gyeongju earthquake. The Pohang earthquake caused one fatality, injured 82 people, and generated more than $300 millions in total economic loss (Ellsworth et al., 2019; Lee et al., 2019). The hypocenter was located approximately 10 km northeast of Pohang city, close to the Pohang Enhanced Geothermal System (EGS) site (36.106°N, 129.373°E and depth ~4.27 km, Korean Government Commission, 2019). Its proximity to the EGS site and hypocentral depth similar to the open hole sections of the fluid-injection wells (Figure 1) quickly raised questions if this earthquake is associated with EGS activities (Grigoli et al., 2018; Kim et al., 2018).

The Pohang EGS project was designed to create an enhanced geothermal reservoir within a low permeability crystalline basement. The basement is overlain by cretaceous volcanic and sedimentary rocks, tertiary volcanic and sedimentary rocks, and quaternary sediments (Ellsworth et al., 2019). During a period of four years (2012 to 2016), two geothermal wells, PX-1 and PX-2 (maximum depth ~4.3 km) were drilled for hydraulic stimulations. At the surface, both wells are separated by only 6 m distance, increasing to a separation of 599 m at a depth of ~4300 m. For well PX-1, the drilling was stuck at a depth of 2419 m, and hence side-tracked into west-northwest direction. Well PX-2 experienced large mud loss in the depth interval 3830 - 3840 m, while cuttings contain significant fractions of friable round-shaped mud balls typical for fault gouge (Korean Government Commission, 2019; Ellsworth et al., 2019). In these geothermal wells, five hydraulic stimulations were conducted between 29 January 2016 and 18 September 2018. During this period, each hydraulic stimulation phase was associated with seismicity. The magnitudes during and after stimulations reached up to $M_L \approx 3$, while events were distributed within a restricted area close to the wells (Woo et al., 2019). The depth of the seismicity before the Pohang earthquake spans the depth range 3.8 to 4.4 km, comparable with the open-hole section of the well at ~4.3 km depth (Ellsworth et al., 2019).

Recent studies confirm that the Pohang earthquake was induced by hydraulic stimulation and extensive fluid injection at this EGS site (Korean Government Commission, 2019; Ellsworth et al., 2019; Woo et al., 2019; Kim et al., 2020). These activities are considered to have activated the previously unmapped fault which was found to intersect well PX-2 at a depth of ~3.8 km. Chang et al. (2020) point out that increased pore-pressure stressing due to multiple injection wells at the Pohang EGS site may have contributed to the mainshock generation. However, it has been argued that the size of fluid-injection induced earthquakes can be managed by controlling pressure,

rate, and location of fluid injection (Hofmann et al., 2019). Data-driven empirical and numerical studies have shown that the largest induced earthquakes are bounded by a function of injected volume (McGarr, 2014; Galis et al., 2017).

Grigoli et al. (2018) find a complex-source mechanism for the Pohang earthquake with a significant non-double couple (non-DC) component. They hypothesized that this earthquake involved failure on two different faults with slightly different focal mechanisms. In fact, in EGS reservoirs with extensive fluid injection and hydraulic stimulation, earthquakes with pronounced non-DC components may occur (Julian et al., 1998). Moreover, fluid injections may induce local deviation of the stress state from the regional stress regime (Schoenball et al., 2014; Martínez-Garzón et al., 2013; Martínez-Garzón et al., 2014). Therefore, we examine how regional and local stress conditions acting on different fault models (single plane and two planes) determine the dynamic rupture process that leads to a source mechanism with non-DC components.

Dynamic rupture modeling aims to reproduce the physical processes that govern how earthquakes start, propagate, and stop for given stress and frictional conditions acting on fault surfaces. The earthquake dynamics are then a result of the model's initial conditions, such as geometry and frictional strength of the fault(s), the tectonic stress state, the regional lithological structure, and a frictional constitutive equation. Jin and Zoback (2018) model coseismic fully dynamic spontaneous fault rupture resulting from preseismic quasi-static loading exerted by fluid perturbations in a faulted porous medium in 2D. Duan (2016) model 2D dynamic rupture accounting for fluid effects of a propagating hydraulic fracture. Cappa and Ruitquist (2012) and Buijze et al. (2017) constrain the onset of 2D dynamic rupture experiments by the stress state resulting from solving a coupled quasi-static poroelastic equation. Further 2D studies that model induced (not fully dynamic) earthquake rupture linked to separately treated fluid diffusion

93 including Galis et al. (2017); Kroll et al., (2017); Dieterich et al. (2015); Garagash and
94 Germanovich (2012); Richards-Dinger and Dieterich (2012); Viesca and Rice (2012). Using
95 modern numerical methods and advanced hardware, a high degree of realism can be reached to
96 explicitly model in 3D the highly non-linear dynamic rupture process (e.g., Heinecke et al., 2014;
97 Roten et al., 2014; Uphoff et al., 2017; Wollherr et al., 2019; Ulrich et al., 2019a, 2019b). The
98 modeling results include spatial and temporal evolution of earthquake rupture, surface
99 displacements, and ground shaking caused by the radiated seismic waves.

100 In this study, we investigate the dynamic rupture process under variable stress and fault-
101 geometry assumptions for the Pohang earthquake, using the high-performance-computing (HPC)
102 enabled software package SeisSol (https://github.com/SeisSol/SeisSol). Two alternative fault
103 geometries are considered, a one fault plane model (Model 1F) and a two fault planes model
104 (Model 2F). In our simulations, we consider a 1D velocity structure (Woo et al., 2019), off-fault
105 plasticity (Wollherr et al., 2018), depth-dependent bulk cohesion, a rapid velocity weakening
106 friction law, borehole estimates of stress, complex fault geometry, and high-resolution topography.

107 In the following, we first describe (Section 2) a new observationally guided fault
108 reconstruction approach based on spatio-temporal clusters of microearthquakes and their spatial
109 uncertainty. In Section 3, we analyse initial fault strength and loading stresses using static and
110 dynamic rupture modeling. We then compare the dynamics and kinematics of two preferred
111 models, Model 1F and 2F. The validation of Model 2F with regional waveforms, as well as
112 comparison of surface deformation between Model 1F and Model 2F are also presented in Section
113 3. Finally, we discuss the importance of considering local stresses loading, apparently weak and
114 critically stressed faults, overpressurized fluids, and dynamic multiple fault interaction in EGS.
115

2. Modeling Setup

In the following, we describe our approach to produce a physically viable model constrained by observational data. Dynamic rupture propagation is governed by fault strength, fault geometry, subsurface material properties, topography, loading ("initial") stresses, nucleation procedure, and empirical friction laws (Dunham et al., 2011a; Harris et al., 2011; Harris et al., 2018). Numerical experiments that vary the aforementioned parameters provide insights into fundamental earthquake physics as well as serve to identify preferred, self-consistent scenarios that explain the mechanical processes of the earthquake as well as observational data.

2.1 Fault reconstruction

The detailed fault geometry has a strong effect on the dynamic rupture process. Changes in strike, dip, and deviations from fault planarity can impact the rupture propagation and the corresponding physical processes. The Pohang earthquake occurred on one or several blind and unmapped fault(s). Because the unwrapped InSAR surface-displacement data show unclear fringes due to the small deformation around the epicenter (Choi et al., 2019; Song and Lee, 2019), we use the high-resolution earthquake catalog from Kim et al. (2018) to constrain the fault geometry based on a space-time (including their uncertainties in space) clustering approach. The earthquake catalog spans from 9 hours before to 3 hours after the mainshock and contains 217 events.

2.1.1 Spatio-temporal clustering

Clustering techniques allow deciphering complex fault structures by associating seismic events to groups (clusters), also discriminating events that are associated with the mainshock from uncorrelated earthquakes. We examine the seismic sequence to separate seismic clusters and

background events using nearest-neighbor distances following Zaliapin and Ben-Zion (2013). The dependence of an event i to a parent event j is determined from the nearest-neighbor distance η_{ij}:

$$\eta_{ij} = dt_{ij} \times dr_{ij}{}^{d}\,, d_{ij} > 0;\ \eta_{ij} = \infty, dt_{ij} < 0 \qquad (1)$$

where $dt_{ij} = t_j - t_i$ is the time between event *i* and *j*, $dr_{ij} = (r_j - r_i)$ is the interevent distance between events; r_i = coordinate of event i and r_j= coordinate of event j, and d is the fractal dimension of the earthquake hypocenter distribution (Hirata, 1989). We find that the inferred clusters are not very sensitive to the parameter d; hence we set $d = 1.6$ following previous studies (Zaliapin and Ben-Zion, 2013; Zhang and Shearer, 2016; Cheng and Chen, 2018). Based on this analysis, we find that all earthquakes of the catalog are part of the cluster and can be used for fault-plane fitting (see Figure 2a). This cluster is characterized by interevent distances less than 1 km.

2.1.2 Fault plane fitting

We adopt the anisotropic clustering location uncertainty distribution (ACLUD) method, a fault-network reconstruction approach introduced by Wang et al. (2013), which accounts for uncertainties in earthquake locations. This method is extended by considering regional tectonic constraints, focal mechanisms, and surface geological manifestation as prior information, leading to the following improvements in the original ACLUD algorithm:

1) Initialize N_0 number of faults following the predefined orientation of the S_{Hmax} extracted from the world stress map with random position and size.

2) For each cluster, if more than four similar focal mechanisms (strike, dip, rake) are available, we use this information to separate events that have distinct focal mechanisms into other clusters.
3) If surface geological manifestation (fault traces) exists (not the case for this study), the strike and dip of the generated fault segment(s) should follow the closest interpreted fault trace orientation.

We refer to this modified ACLUD method as guided-ACLUD (g-ACLUD).

All explored solutions are subject to a statistical validation process that examines the likelihood of each proposed fault-network, given all available focal mechanisms. Statistical validation uses the Bayesian Information Criterion (BIC). Initially, the method uses a random number of fault planes. A single fault plane may be split if the BIC remains high. On the other hand, two close-enough fault planes with similar orientation (strike and dip) may be merged into a single fault plane. The process is repeated until the BIC reaches a pre-defined minimum or if the process exceeds the maximum specified number of iterations (Wang et al., 2013).

The ACLUD algorithm by Wang et al. (2013) uses event locations and the associated uncertainties given by the earthquake catalog. We incorporate additional information to increase the robustness of the results and to decrease the explored parameter space. As *a priori* information, we use the orientation of the maximum compressive regional stress given by the world stress map (Heidbach et al. 2018) and available focal mechanisms in the area which are associated with the earthquake catalog. Therefore, we use a maximum horizontal stress orientation of 74° with an uncertainty of 25° and consider the focal mechanism inferred by Grigoli et al. (2018). Since location errors are not specified in this earthquake catalog, we assume normally distributed uncertainty for all events (standard deviation of 100 m). Note that Kim et al. (2018) obtained a

183 median error of 42, 31, and 36 m in the EW, NS, and vertical directions, respectively, but no
184 uncertainties for individual events.

185 Figure 2b, 2c, 2d show the g-ACLUD selected solution, characterized by the smallest BIC,
186 which features two intersecting planar fault planes. The main plane strikes at 214° and dips at 65°,
187 while the secondary fault plane strikes at 199° and dips 60°, respectively. The two fault planes are
188 separated by a narrow angle of 15°. The secondary fault aligns with the subsidiary fault plane
189 identified by Kim et al. (2018). The dimensions of the main and secondary fault planes are 4.3 x
190 2.8 km and 3.0 x 2.2 km, respectively. As the goal of this study is to compare the rupture process
191 for two different fault configurations, we define a one fault plane geometry (Model 1F) and a two
192 fault planes geometry (Model 2F; derived fault reconstruction analysis). The single-fault model
193 has a fault plane striking 214° and dipping 43°, as suggested by Korean Government Commission
194 (2019), Ellsworth et al. (2019), and Woo et al. (2019).
195

196 ## 2.2 Material properties

197 We assume an elasto-plastic, isotropic medium based on the 1D velocity profile (Figure
198 S1a; Woo et al. (2019)). The velocity profile honors geological structures observed from drilling
199 cores and seismological observations from both active and passive sources, for instance, vertical
200 seismic profiling (VSP) and well logging (Korean Government Commission, 2019; Woo et al.,
201 2019). The density distribution (Figure S1a) is adopted from the report by Korean Government
202 Commission (2019).

203 We use a computationally efficient implementation of a Drucker-Prager off-fault
204 viscoplastic rheology (Wollherr et al., 2018). The off-fault failure criterion is based on the internal
205 friction coefficient (bulk friction) and bulk cohesion. We assume a constant internal friction

coefficient equal to the prescribed on-fault friction coefficient ($\mu_{bulk-friction} = 0.6$) for the entire model domain. However, bulk cohesion is set to be depth-dependent, accounting for geologic strata in the Pohang EGS site and the hardening of rocks with depth. Therefore, bulk cohesion ranges from $c = 4$MPa near the surface to $c = 50$MPa at a depth of 6 km. A lower bulk cohesion (12.5% of the surroundings) is applied in a 1.5 x 0.3 x 4 km^3 volume around the fault intersection for the case of two fault planes to mimic pre-existing damage which enhances off-fault yielding and to prevent unrealistic high on-fault stresses at the fault intersection. We assume initially equivalent stresses acting on and off the fault. Finally, we set a constant, mesh-independent relaxation time following the analysis by Wollherr et al., (2018) and chose T_V= 0.05 s, consistently with choices made in previous studies (e.g. Ulrich et al., 2019a, 2019b).

2.3 Fault strength and loading stresses

To constrain the most viable principal stress component azimuth and the overall stress regime, we extract information (e.g., S_{Hmax} orientation and fault strength) from laboratory and field observation to then perform numerical experiments. We adopt a friction law with rapid velocity weakening (adapted from Dunham et al., 2011a; see Appendix A1) which reproduces the rapid friction decrease observed in laboratory experiments at co-seismic slip rates (Di Toro et al., 2011).

We parametrize fault friction aiming for realistic levels of static and dynamic frictional resistance and stress drop. All frictional properties are detailed in Appendix A1. We apply velocity weakening ($b - a = 0.004$) across the fault (see Figure S1b) and velocity strengthening ($b - a = -0.004$) to the uppermost part of the fault, which allows for a smoother termination of the rupture there. The state evolution distance (L), initial slip rate (V_{ini}), reference slip velocity (V_0), steady-

229 state friction coefficient (f_0), and weakened friction coefficient (f_w) are constant and depth-
230 independent.

231 We follow the systematic approach of Ulrich et al. (2019a) to examine initial fault stress
232 and relative apparent fault strength combining data from observations, (e.g., seismo-tectonic
233 observations and fault fluid pressurization) and the Mohr-Coulomb theory of failure. This
234 workflow reduces the non-uniqueness in dynamic rupture modeling parameterization by assessing
235 that the stress state is compatible with the fault geometry and the fault-slip orientation (rake angle)
236 inferred from finite source or moment tensor inversion. Assuming an Andersonian stress regime
237 (one principal stress axis is vertical), only four parameters are sufficient to fully describe the stress
238 state and strength of the fault system: the azimuth of maximum compressive stress (S_{Hmax}), the
239 initial relative fault prestress ratio (R_0), the stress shape ratio (ν), and the fluid pressure ratio (γ),
240 all detailed hereafter.

241 The Pohang EGS site is considered to be located within a strike-slip stress regime (Soh et
242 al., 2018, and references therein). This translates into the maximum principal stress being
243 horizontal ($s_1 = S_{Hmax}$, with principal stress components $s_1 > s_2 > s_3 > 0$) under Andersonian
244 stress. Previous studies examined the azimuth of maximum horizontal stress using different
245 methods, such as borehole and seismological techniques, e.g., stress inversion of focal mechanisms
246 (Kim et al., 2017; Lee et al., 2017; Lee, Hong, and Chang, 2017; Soh et al., 2018; Korean
247 Government Commission, 2019; Ellsworth et al., 2019). Soh et al. (2018) inferred S_{Hmax} from
248 focal mechanisms of earthquakes that occurred between 1997 and 2016 and determined a regional
249 $S_{Hmax} = 74°$. However, the earthquakes closest (~40 km) to the Pohang EGS site used in their
250 analysis are the 2016 Gyeongju event and its aftershocks. Based on borehole data, Kim et al. (2017)
251 and Lee, Shinn, et al. (2017) determined thatS_{Hmax} at shallow depths (700 m to 1000 m) within a

10 km radius from the Pohang EGS is about 130°. In contrast, Ellsworth et al. (2019) and Korean Government Commission (2019) inferred a critically stressed thrust faulting regime. This stress state implies that the vertical stress is the least principal stress under Andersonian stress ($s_v = s_3$). They inferred an S_{Hmax} orientation of $77 \pm 23°$ based on dipole sonic logging data. This orientation is similar to the value of 74°given in the world stress map (Heidbach et al., 2018).

Using numerical simulations, we then assess how these loading-stress regimes for the inferred fault geometry determine nucleation and rupture of the Pohang earthquake. The stress shape ratio ν enables a contrast of different stress styles by balancing the principal stress amplitudes. It is defined as:

$$\nu = \frac{(s_2 - s_3)}{(s_1 - s_3)} \qquad (2)$$

For strike-slip regimes (s_2 vertical), $\nu < 0.5$ characterizes transpression, $\nu \approx 0.5$ corresponds to pure strike-slip regime, and $\nu > 0.5$ characterizes transtension (Ulrich et al., 2019a). Soh et al. (2018) (ν= 0.12), Ellsworth et al., (2019) and Korean Government Commission (2019) ($\nu = 0.1$) suggests a stress regime acknowledging transpression around the Pohang EGS site (note that they use different definition of ν).

The initial relative prestress ratio (R_0) describes the closeness to failure on a virtual, optimally oriented fault. $R_0 = 1$ indicates a critical stress level on all optimally oriented faults. We can characterize fault strength spatially by calculating the relative prestress ratio (R) on every point of the fault. R denotes the ratio of potential stress drop $\Delta\tau$ with respect to breakdown strength drop $\Delta\tau_b$ for given frictional cohesion (c), static (μ_s) and dynamic (μ_d) friction coefficient (e.g., Aochi and Madariaga, 2003) expressed as:

$$R = \frac{\Delta\tau}{\Delta\tau_b} = \frac{\tau_0 - \mu_d\sigma_n}{c + (\mu_s - \mu_d)\times\sigma_n} \quad (3)$$

where τ_0 and σ_n are initial shear and normal traction on the fault plane, respectively. However, in this study, we neglect the contribution of frictional cohesion ($c = 0$), which is mostly important to incorporate close to the Earth's surface. We assume $\mu_s = f_0 = 0.6$ and $\mu_d = f_w = 0.1$. The relative prestress ratio can be related to the relative fault strength parameter (S) defined as $S = 1/R - 1$. On-fault values of R change at every point as we vary R_0, taking on values $R \leq R_0$ depending on the orientation of each fault point with respect to the optimal orientation.

The vertical principal stress is assumed to vary linearly with depth, consistent with the geological strata (depth-dependent density (ρ) in Figure S1a). We assume the intermediate principal stress component, s_2, to be vertical. The confining pressure of the overlying rock is reduced by the pore pressure (P_f). We assume P_f proportional to lithostatic stress as $P_f = \gamma\rho g z$, where g is the gravitational acceleration (9.8 m/s^2), and z denotes depth (in meters) and γ is the fluid pressure ratio. A fluid pressure ratio of 0.37 indicates hydrostatic pore pressure, while $\gamma > 0.37$ implies an overpressurized stress state.

We perform a range of static and dynamic numerical experiments described below to test the sensitivity of the resulting dynamic rupture models to the chosen stress parameterization in terms of S_{Hmax}, R_0 and γ. We keep the 4th parameter, the stress shape ratio, fixed at $\nu = 0.12$ (Soh et al., 2018). We do not adjust the stress states for the stress excess during nucleation (see Appendix A2). The overstressed nucleation and its parameters are constant for all 180 numerical experiments.

3. Results

We use the open-source software SeisSol (details in Appendix A3, **numerical method**) to solve the elastodynamic equations of motion for fault rupture under stress and friction acting on the fault surface, coupled to seismic wave propagation in complex media. We set the on-fault mesh size using estimates of cohesive zone width (details in Appendix A3, **mesh generation**). We incorporate high-resolution topography into our modeling. Figure 3 shows the computational mesh overlain by a snapshot of absolute velocity at t = 5 s.

Next, we present 3D dynamic rupture simulations for scenarios that consider one and two intersecting fault planes, incorporating depth-dependent regional loading stresses, off-fault plastic yielding, and high-resolution surface topography. In the preferred model (Model 2F), the secondary fault plane is dynamically triggered and can explain the observed non-double couple component of the moment tensor solution. Our model is compatible with regional waveforms and surface deformation derived from published InSAR analysis.

3.1 Static and dynamic analysis of initial fault strength and stresses

We first constrain the regional stress from purely static analysis. Figure S2 shows a few cases (out of many permutations (see also Table S1)) we analyzed. The six examples shown use parameters $\gamma = 0.5$ and $R_0 = 0.7$, and variable S_{Hmax} in the range 52° - 140°. According to the static analysis, $S_{Hmax} < 87°$ is insufficient to generate a rake angle of shear traction compatible with the thrust-faulting component inferred by the focal mechanism and moment tensor solution. At $S_{Hmax} \geq 87°$, a thrust-faulting component starts to emerge. Interestingly, only the secondary fault plane features a rake angle larger than 40° for $S_{Hmax} = 77° - 140°$. A rake angle of ~ $80°$, obtained with $S_{Hmax} = 120°$, can potentially produce the thrust-faulting component inferred by

moment tensor solution. For this parametrization, the secondary fault plane reaches a higher rake angle of approximately 110°.

We restrict the parameter space for R_0 and γ based on our static analysis. We then systematically explore all permutations of the three different parameters within the selected range using dynamic rupture simulations. We vary R_0 in the range 0.7 - 0.9, γwithin 0.37 - 0.9 and S_{Hmax} within 67 - 120°. Figure 4 summarizes the outcome of 180 numerical dynamic rupture experiments. We find that under hydrostatic pressure ($\gamma = 0.37$), $S_{Hmax} = 120°$ generates self-sustained ruptures over any other S_{Hmax} orientation.

The thrust-faulting component generated with $S_{Hmax} = 67° - 87°$ is insufficient to explain the seismological observation using dynamic rupture modeling. Such S_{Hmax} leads to pure strike-slip faulting as the only mechanical viable solution. Both dynamic and static analyses suggest that $S_{Hmax} = 120°$ is necessary to generate a thrust-faulting component close to the observations. Our analyses allow determining a preferred parameterization, compatible with inferred ground deformation, observed regional waveforms, and the inferred focal mechanism: $R = 0.8$ and $\gamma = 0.5$.

3.2 Rupture dynamics of the preferred scenario Model 1F and Model 2F

Figure 5a and movie M1 (in supplementary material) provide an overview of the simulated earthquake rupture of the preferred two fault model Model 2F: rupture propagates spontaneously across the main fault plane and dynamically triggers the secondary fault plane (rupture jumping).

The rupture nucleates smoothly due to the prescribed time-dependent overstress (see Appendix A2) centered at the hypocenter location; it then spontaneously propagates bilaterally across the main fault plane. At a rupture time of 0.65 s, two successive slip-rate fronts emerge,

with lower peak slip rates than the main rupture front (Figure 5a, left). This rupture complexity is associated with the simultaneous rupture on both fault planes, leading to multiple reflected and trapped waves in-between the two fault planes, reactivating the main fault around the intersection. Rupture complexity decreases as rupture on the secondary fault plane terminates. After rupture time t = 0.75 s, we observe solely pulse-like rupture propagation across the main fault.

The secondary fault plane is dynamically triggered at 0.4 s and its rupture terminates at 0.8 s simulation time, while the main-fault is fully ruptured in about 1.1 s. The secondary fault plane is only partially ruptured because the northern part of the main fault does not slip. High slip-rates (~ 10 m/s) and multiple rupture fronts occur near the fault intersection at the secondary fault. Rupture heals close to the fault intersection region around $t = 0.65\ s$.

After $t = 0.75\ s$ rupture on the main fault dynamically clamps (e.g., Kyriakopoulos et al., 2019) and thus does not facilitate direct branching to the northern unbroken part of the secondary fault plane. We observe asymmetric peak slip-rate distribution (see Figure S3), with higher values on the single fault plane part of the network (Figures 5a, right) and lower peak slip rates where ruptures across directly adjacent fault planes interact, which is also associated with high off-fault plastic yielding (see section **Off-fault deformation** below). The entire rupture is completed after ~1.5 s simulation time, breaking 4 km of fault length and generating a moment magnitude of M_w 5.59 (dominated by slip on the main fault plane). We find that rupture stops smoothly and spontaneously on the secondary fault plane and north-eastern part of the main fault plane, while being stopped abruptly by the southwestern fault end of the main fault plane.

In contrast to the Model 2F, the one fault plane preferred Model 1F produces symmetric bilateral slip-rate and slip distributions.

3.3 Rupture kinematics of the preferred Model 1F and Model 2F scenarios

Due to the size of the event and limited available data, the kinematics of the Pohang earthquake are challenging to characterize and explain. We here describe the model kinematics of the preferred Model 1F and Model 2F earthquake scenarios. and compare both with two observational studies (Song and Lee, 2019; Grigoli et al., 2018).

Song and Lee (2019) estimated the static slip distribution by InSAR (both descending and ascending-descending orbit) for a single fault plane with patch size 0.5 by 0.5 km. Higher slip predominantly occurs northeast of the hypocenter, with an average slip of 0.15 m (Song and Lee, 2019). Grigoli et al. (2018) applied an Empirical Green's Function (EGF) technique to study rupture duration and directivity, suggesting an apparent rupture duration of ~1s and ~3 s for stations observed in the SE and NW direction, respectively. Their focal mechanism shows an average rake of ~135°.

Both preferred scenarios vary slightly in moment magnitude, $M_W\ 5.63$ and $M_W 5.59$ for Model 1F and Model 2F, reflecting different fault geometries while otherwise using the same dynamic rupture model parametrization. We point out that most slip of Model 2F occurs on the main fault - its magnitude is reduced to $M_W 5.51$when removing the subsidiary plane.

The resulting synthetic source time functions of Model 1F and Model 2F are presented in Figure 7a and 7b, respectively. The boxcar shaped moment rate function of Model 1F results from its comparably simple rupture dynamics across one planar fault. Model 2F features a more complicated moment rate function featuring two peaks of which the first one is reached at t = 0.5 s simulation time during simultaneous rupture of both fault planes. The rupture duration of both scenarios is less than 1.5 s. The moment tensor representations of Model 1F and Model 2F are presented in Figure 7c and 7d, respectively. Both scenarios show oblique faulting mechanisms.

Model 1F clearly produces a double-couple moment tensor solution (Figure 7c), whereas the Model 2F yields a non-double couple solution due to complex source mechanism (Figure 7d), in agreement with Grigoli et al. (2018). Nevertheless, our simulation produces a smaller amount of CLVD (compensated linear vector dipole) compared to Grigoli et al. (2018). In fact, the equivalent moment tensor solution of Model 2F can be decomposed, following the methodology of Vavryčuk (2015), into 82.95% DC, -5.05% CLVD, and -12% isotropic (ISO) components. In contrast, Grigoli et al. (2018) find -37% CLVD. In our simulations, Model 2F's rupture is characterized by an average rupture speed of $v_r \approx 2{,}250\, m/s$, well below the average Rayleigh wave speed at the depth of the faults ($v_r \sim 0.75 V_S$). The spatial variation of v_r is mainly related to the complexity of rupture around the intersection for both, the main and secondary fault plane. We observe higher average rupture speed $v_r \approx 2{,}780\, m/s$ ($v_r \sim 0.8 V_S$) on the secondary fault plane (see rupture contours every 0.2 s in Figures 5a, 5b). We note the localized occurence of supershear rupture speeds ($\sim 4000\, m/s$) near the edge of the prescribed nucleation patch of the main fault reflecting the high overstress required for initiating the preferred rupture dynamics in our setup. Also, the secondary fault plane features localized supershear episodes ($\sim 3800\, m/s$). In our model setup, this may be translated into locally high fluid overpressure, and/or reflect the low resolution and 1D restriction of the used velocity model. More complex fluid effects have been shown to transition sub-rayleigh to supershear ruptures in fully coupled 2D models by Lin and Zoback (2018).

In our preferred model, high slip ($\sim 2\, m$) occurs in the center of the main fault. We observe a maximum slip of 1.3 m at the secondary fault plane (Figure 6b). In total, the average on-fault slip is 0.32m. Both, Model 1F and Model 2F, feature higher slip than Song and Lee (2019) infer in their static slip inversion. In addition, differences may arise due to different modeling

assumptions in terms of fault dimensions and shear moduli. First, Song and Lee (2019) assume a slightly larger shear modulus of G = 30 GPa than in our model (G = 26 GPa). Second, they assume a single fault plane of significantly larger dimensions (6 x 5 km) than the faults of our models (see section **Fault reconstruction**). This large fault geometry allows for the possibility of near-surface slip.

The orientation of fault slip is modulated by the dynamic source process. The dynamic interaction of the two fault planes induces a moderate thrust-faulting component (rake $\sim 135° - 150°$) on the main fault plane, as well as complex time-dependent rake orientations on the secondary fault (see also Figure 6c, 6d). In contrast to Model 2F, the orientations of the final rake angle of Model 1F are distributed homogeneously, on average at 127°. The rake of Model 1F is different from Model 2F due to different dip angles of the main fault which dips at 43° in Model 1F. This average rake angle is comparable to the focal mechanism derived by Grigoli et al. (2018). The average on-fault slip is 0.35 m. We observe that, on average, the rupture speed is $v_r \approx 2400$m/s. Reflecting similar dynamic parameters to Model 2F, Model 1F also experiences supershear rupture near the nucleation patch.

3.4 Waveform comparison for Model 1F and Model 2F

In the following, we analyze the differences between Model 1F and Model 2F in terms of near and far-field ground motion. Hereinafter, all distances from the fault are considered as Joyner-Boore distances (R_{JB}, the shortest distance from a site to the surface projection of fault planes). We compare synthetic waveforms computed for hypothetical ("virtual") stations located close (~4 km) and far (>20 km) from the epicenter.

Figure 8b shows three-component waveforms at 19 randomly located virtual stations (Figure 8a). We place 10 stations near the epicenter (~4 km horizontal distance) to inspect near field seismic waveform characteristics. We filter all synthetic waveforms within the frequency band of 0.1 - 2 Hz using a fourth-order Butterworth filter. Figure 8c depicts all 3-component velocity waveforms. Overall, waveforms of scenarios Model 1F and Model 2F are very similar in this frequency range, but waveforms from Model 1F have systematically higher amplitudes than Model 2F. The most remarkable amplitude differences occur on the EW component for stations 004, 008, 009, and 010, which are all located above or close to the faults.

At some stations, distinct waveform differences appear (e.g., the NS-component of stations 007, 014, 011, and 019). Most of these stations are located on the hanging wall. After five seconds, once the rupture is fully arrested, differences vanish, and the waveforms become comparable for both models. As depicted in Figure 8b, the stations located close to the region where faults overlap in Model 2F show significant differences in seismic wave signatures on the horizontal components. One possible explanation may be that the additional secondary fault defocuses ground motions.

3.5 Off-fault deformation

Our preferred dynamic earthquake rupture model 2F reveals significant off-fault plastic deformation in the vicinity of geometric fault complexity, similar to scenarios of the 1992 Landers earthquake (Wollherr et al., 2018), the 2016 Kaikoura earthquake (Klinger et al., 2019) and the 2019 Ridgecrest earthquake sequence (Taufiqurrahman et al., 2019). Here, significant off-fault plastic deformation (quantified as the scalar quantity η following Ma, 2008 and Wollherr et al., 2019) occurs (i) in the pre-existing damage zone at the fault intersection, (ii) at the dilatational side of the main and the secondary fault as expected from previous theoretical and numerical studies,

458 given the shallow angle of both faults and S_{Hmax} (Templeton and Rice, 2008; Gabriel et al., 2013),
459 and (iii) close to the free-surface (see Figures S3c and S3d).

460 The fault intersection of Model 2F elevates the total off-fault plasticity response
461 regularizing high on-fault stresses while limiting peak slip rates and reducing peak ground motions
462 (Andrews 2005; Dunham et al. 2011a; Gabriel et al., 2013; Roten et al., 2014; Wollherr et al.,
463 2018). When comparing waveforms, we indeed notice overall lower velocity amplitudes compared
464 to Model 1F in the surrounding stations of the fault planes caused by the combined effects of fault
465 complexity and off-fault yielding. Interestingly, the stronger plastic yielding response in model 2F
466 leads to lower variability (not shown here) in ground motions (PGV) (as in Wollherr et al., 2019)
467 even though the fault geometry is more complex.
468

469 ## 3.6 Model 1F and Model 2F surface deformations

470 Next, we compare the co-seismic surface displacement generated by Model 1F to Model
471 2F (Figure 9a, 9b). We translate the synthetic vertical and horizontal displacements into Line-of-
472 sight (LoS) displacement components.

473 The spatial distribution of the co-seismic surface deformations is noticeably different.
474 Model 1F features higher LoS displacements in southeastern direction relative to the Gokgang
475 Fault (~ *2 km* from the bay) compared to Model 2F (~ *5 km* from the bay) and generates on
476 average lower negative LoS displacements. Model 1F creates a wider area of uplifted LoS
477 displacements, which resembles an ellipse with a major axis of 6 km and a minor axis of 4.1 km.
478 The most prominent spatial differences are (i) the vertical LoS displacements of Model 1F are
479 slightly migrated to the East relative to the epicenter and (ii) the location of zero displacements in
480 between vertical LoS displacements (in the region of the epicenter) and negative LoS

displacements at the eastern-to-southward of the epicenter. Model 2F produces an average of 5 cm subsidence whereas Model 1F only produces 2 cm average subsidence. This can be attributed to Model 1F's more shallow dipping angle. The co-seismic surface displacements of Model 2F compare better than those of Model 1F to InSAR ground deformation inferences of Song and Lee (2019), in terms of the location of the pivot line delimiting positive and negative LoS displacements (~ *4.5 km* from the bay).

While synthetic (Model 2F) and observed surface displacements significantly differ locally and quantitatively, they reveal qualitatively comparable large-scale features. The following observations are captured by Model 2F: (i) Uplift/easting displacement is observed near the epicenter and (ii) the uplifted area forms an ellipse-like shape with a major axis of ~5.6 km and a minor axis of ~3.8 km. Correspondingly, Pohang city also experienced subsidence according to field observations (Kang et al., 2019a, Kang et al., 2019b). Additionally, our synthetics also suggest subsidence underneath the bay.

Although the contribution of the secondary fault plane is critical to reproduce the inferred non-DC component, comparison of synthetic co-seismic surface displacements of Model 2F with and without the secondary fault (see Figure S5a) suggests that the contribution of the secondary fault plane to the ground displacement is small (Figure S5b), as expected from its small slip contribution. We note that the InSAR data may not be sensitive enough to discriminate between a one and a two-fault plane model.

3.7 Model 2F validation by regional waveform modeling

Unfortunately, a local seismic network of eight portable seismic stations (Kim et al., 2018) deployed around the EGS site produced saturated (clipped) seismograms. Therefore, we choose to

compare synthetic waveforms to regional recordings at five stations surrounding the Pohang EGS site (see Figure 1) at epicentral distances of approximately 70 km.

Model 2F compares well to regional low-frequency seismic wave observations (Figure 8c). Synthetic waveforms are calculated using a Green's function database of teleseismic waveforms (Instaseis, Krischer et al., 2017). We translate the dynamic rupture model into a single moment tensor representation following Ulrich et al. (2019a, 2019b). The Green's function database we use is based on the anisotropic Preliminary Reference Earth Model (PREM), and is accurate to a maximum period of 2 s. Synthetic and observed waveforms are filtered using a 0.033 - 0.08 Hz 4^{th} order Butterworth filter, equivalent to the frequency band used in the source inversion of Grigoli et al. (2018). The goodness of fit is assessed by the root-mean-square (rms) misfit.

Although the synthetic waveforms compare reasonably well to regional recordings, we find that a few synthetic amplitudes are systematically larger than the observed data. We attribute this to the usage of a 1D PREM model, which is more suitable for modeling synthetics at larger azimuthal distance. Additionally, the fact that our simulation returns a slightly higher seismic moment than observed and is not able to capture the full non-DC component of the source may play a role. In particular, the large misfit at Station TJN on the UD and EW component may be attributed to unmodeled site effects. Our synthetics do not differ significantly from the synthetics of Grigoli et al. (2018), derived by full-waveform inversion of the waveforms recorded at stations BUS2, CHJ2, and NAWB. A significant difference is only noticeable on the NS component of station BUS2 (south of the epicenter, Figure 1).

4. Discussion

4.1 The importance of local stresses for rupture dynamics in EGS

The inferences of previous studies vary in terms of stress regimes and maximum horizontal stress orientation around the Pohang EGS site, thereby motivating our systematic numerical experiments as detailed in section **Static and dynamic analysis of initial fault strength and stresses** under various loading stress settings. Assuming an Andersonian stress regime, we find that an initial stress state constrained by regional stress inversions is unable to generate the observed thrust-faulting component of the Pohang earthquake. This suggests important local deviations from the regional stress state near the Pohang EGS site. Kim et al. (2017) and Lee et al. (2017) infer the stress orientation at short epicentral distance (< 10 km) from borehole image log data acquired prior to the Pohang earthquake. However, this data is limited to 1 km depth, whereas the Pohang earthquake hypocentral depth is inferred to be deeper, at a depth of 4.27 km. Ellsworth et al. (2019) noted that the in-situ stress state at the Pohang EGS site is transpressional.

From our static numerical experiments, we infer that a pure strike-slip stress regime ($s_2 = s_v$) and $S_{Hmax} = 120°$ yield a thrust-faulting component consistent with observations (Figure S2). This finding is corroborated by our dynamic rupture simulations under identical loading (Figure 7c, 7d). We also observe that under these conditions spontaneous rupture propagation is favoured. The reverse faulting regime ($s_3 = s_v$) accounting for low $\nu = 0.1$ was also explored. However, such reverse-stress regime, as suggested by Ellsworth et al. (2019), across the entire fault planes does not yield sufficiently high shear tractions on our fault system - and dynamic rupture dies out quickly.

Local variations of the stress state around EGS sites, including the Pohang EGS site, have been observed in hydraulic stimulation experiments of crystalline-rock reservoirs (Schoenball et a., 2010), data-driven geomechanical analysis (Ceunot et al., 2006; Hardebeck and Michael, 2006; Martínez-Garzón et al., 2013; Martínez-Garzón et al. 2014; Schoenball et al., 2014) and numerical

experiments (Jeanne et al., 2015; Ziegler et al., 2017). Such spatial and temporal stress reorientation is typically a direct response to hydraulic stimulation and fluid injections (Cornet et al., 2007; Schoenball et al., 2010; Schoenball et al., 2013; Ziegler et al., 2017, Liu and Zahradnik, 2019). In the geothermal field surrounding the Geysers in California, Martínez-Garzón et al. (2014) found that the stress regime changed from normal-faulting to strike-slip near the injection wells. At the Pohang EGS site, local variations in the stress regime have been inferred from focal mechanisms of microearthquakes before and after the Pohang earthquake. Woo et al. (2019) reported strike-slip faulting north from the hypocenter to strike-slip associated thrust-faulting and pure thrust-faulting components towards the South before the mainshock. After the mainshock occurred, aftershock focal mechanisms were mainly strike-slip in the SW to oblique faulting in the NE (Kim et al., 2020). Changes in the stress orientation and regime near the hypocenter prior to the mainshock could correspond to hydraulic stimulation and fluid injections (Martínez-Garzón et al., 2014; Liu and Zahradnik, 2019). However, the aftershock source characteristics are probably related to co-seismic stress rotation.

Based on our analysis of various numerical experiments, we deduce that our models are highly sensitive to variations in the initial stress state, and therefore allow to finely constrain the fault stress loading parameters. For example, a small change in S_{Hmax} may induce a significant change in the modeled focal mechanism. All faults are exposed to the same local stress regime while experiencing varying ratios of shear and normal loading depending on their orientation towards this loading. Even a small change in fault geometry (e.g., in strike, dip, size, and the angle between fault planes) strongly affects the dynamic rupture result (e.g., Yamashita and Umeda, 1994; Aochi et al., 2005; Bhat et al., 2007; Ulrich et al., 2019a; van Zelst et al., 2019), as here illustrated when comparing Model 1F and Model 2F. We point out that trade-offs between the

inferred stress state and fault geometry can be readily explored if new observations become available.

In summary, these observations support our assumption on the loading stress, which is consistent with Ellsworth et al. (2019) in the nucleation region, but differently oriented everywhere else. Complexities in the in-situ stress state are expected in the region where the Pohang earthquake occurred, due to the history of hydraulic stimulations, that is, the EGS operation itself perturbs the local stress conditions in a manner that makes it more difficult to assess the potential seismic hazard implication (that are usually studied in advance and utilize regional stress information).

4.2 The importance of critically stressed, static and dynamic weak faults and overpressurized fluids

Our experiments (Figure 4) emphasize the necessity of assuming overpressurized fluids ($\gamma > 0.37$) and a close to critical stress state when assuming strong frictional weakening on the fault(s). A critically stressed state has been suggested by Ellsworth et al. (2019) by analyzing dipole sonic logging data at the Pohang drilling site. In our preferred Model 2F, we use the ratio of shear over effective normal stress (τ/σ_n) to quantify fault strength, and find 0.54 and 0.59 for the main and secondary fault plane, respectively. This fault strength is close to the assumed steady-state friction coefficient ($f_0 = 0.6$) which indicates that the faults are close to failure prior to rupture nucleation and thus close to critically stressed.

In our preferred model both faults are non-optimally oriented with respect to the local stress conditions. The relative prestress ratio R is 0.35 on the main fault and 0.4 on the secondary fault plane, which is less than our assumed R_0= 0.8. According to Andersonian faulting theory, the fault strength is related to its orientation with respect to the regional stress. Here, the main fault plane

is oriented at 54° and the secondary fault at 60° relative to the regional maximum compressive stress (S_{Hmax} = 77°). Thus, the two fault planes system would be considered weak in the classic, static sense.

All modeled faults in this study weaken dramatically at co-seismic slip rates while stress drops are limited by the elevated fluid pressure. Besides resembling the dramatic friction decrease observed in laboratory experiments and the theory of thermal weakening processes, previous dynamic rupture studies utilizing rapid velocity weakening with low values of fully weakened friction coefficient (f_w) reproduced rupture complexities, such as rupture reactivation and pulse-like ruptures, without assuming small-scale heterogeneities.

In our simulation, we use a fluid pressure ratio of 0.5 which corresponds to a reduction of the normal stress of approximately 14.3 MPa compared to a hydrostatic state. The reduction in effective normal stress mechanically lowers the static strength of faults. Our assumption of high fluid pressure may relate to various episodes of drilling mud loss on 30-31 October 2015 at 3800 m depth suggesting an increase of fluid pressure on the order of 20 MPa around the borehole, and the fluid injection operations (Ellsworth et al., 2019; Korean Government Commission, 2019).

4.3 The importance of fault interaction for the dynamic rupture process and faulting mechanism

In our preferred model, the secondary fault is only partially ruptured during the Pohang earthquake. Strong variations in slip rate associated with dynamic rupture complexity across the two faults planes and their interaction, spontaneous rupture arrest and the asymmetrically accumulated fault slip on the main and secondary fault plane, could potentially favor dynamic and static Coulomb stress transfers enabling a later activation of the unruptured area of the secondary

619 fault. The largest aftershock that occurred less than three hours after the mainshock at 650 m
620 epicentral distance to the northwest with respect to the mainshock may have occurred in such an
621 unruptured area on the secondary fault.

622 In our model, complex shear faulting across two fault planes induces a non-DC component,
623 which is, nevertheless, considerably smaller (14%) compared to the CLVD component inferred by
624 Grigoli et al. (2018). Additional factors not considered in this study may contribute to an apparent
625 non-DC component, such as strong deviations from fault planarity (larger scale curvature and
626 small-scale roughness, e.g., Bydlon and Dunham, 2015; Shi and Day, 2013; Ulrich and Gabriel,
627 2017; Mai et al., 2018), stronger heterogeneities in fault stress and strength (Ripperger et al., 2008)
628 and 3D subsurface structure (e.g., Pelties et al., 2015) increasing rupture complexity, as well as
629 incorporating tensile faulting, poroelastic rheology, and source or propagation anisotropy (Julian,
630 1998; Boitz et al., 2018). The CLVD contribution may also increase when assuming a larger
631 number of faults. While the limited data available does not suggest rupture of additional fault
632 planes, stochastically distributed and dynamically activated fracture networks (e.g., Okubo et al.
633 2019; Anger and Gabriel, 2019) around the main fault are expected given the on-going stimulation
634 operation.

635

636 ## 4.4 Importance of dense seismic monitoring during EGS projects

637 The complex interaction of local stress loading and fault strength conditions, rupture
638 dynamics and fault interaction on multiple fault segments presented here highlights the importance
639 of a dense local seismic network within the operational areas for monitoring and analyzing
640 microseismicity before, during, and after EGS operation, to thereby mitigate the potential seismic
641 hazard. Pre-EGS stimulation seismic monitoring is needed to define the ‘unperturbed state’ of the

642 system (the rock volume to be stimulated) and for characterizing potentially unmapped fault(s)
643 that may interact during cascading rupture; such seismic monitoring may be accompanied by
644 detailed borehole logging to assess the local stress state prior to stimulation.

645 During the stimulation and operational phase, a dense seismic monitoring network is also
646 needed to facilitate high-precision and high-fidelity seismic source studies. In conjunction with
647 detailed operational fluid-injection parameters, the reservoir stress state and its susceptibility for
648 generating earthquakes can be assessed (Galis et al., 2017; Kwiatek et al., 2019). In fact, the
649 available recordings of the operational monitoring seismic network near the Pohang EGS site were
650 saturated (clipped) by the unexpected high magnitude earthquake, thus accelerometers would be
651 useful as complementary instruments in EGS monitoring networks. In addition, the rise of
652 Distributed Acoustic Sensing (DAS) opens new opportunities as an additional seismic monitoring
653 network especially for EGS that is located in urban areas (Zhan, 2019).

654 Our study suggests that fully physics-based numerical simulations prior, during and after
655 an EGS project may be useful to not only gain a first-order understanding of potential effects and
656 consequences of the EGS experiments (e.g., risk-prone area as reflected by peak ground motions
657 (PGVs, Figure S6)), but also to optimally design the seismic monitoring network to ensure that all
658 vital data are collected as needed for future monitoring and mitigation purposes.

659

660 5. Conclusions

661 A guided fault reconstruction approach that clusters spatio-temporal aftershock locations
662 accounting for their uncertainty is applied to create a two fault planes dynamic rupture model
663 which reproduces key characteristics of the Pohang earthquake. Rupture complexity is arising from
664 the dynamic interaction of two failing fault planes with shallow intersection angles.

Static Mohr-Coulomb failure analysis and 180 numerical simulations demonstrate that the regional loading stress is unable to generate dynamic rupture consistent with the observed faulting style. Resolving the regional tectonic stress field onto one fault of a geometry as suggested by Korean Government Commission (2019), Ellsworth et al. (2019), and Woo et al. (2019) or onto the reconstructed two fault planes leads inevitable to pure strike-slip faulting, in stark contrast to the observed thrust-faulting mechanism. Instead, local stress variation relative to regional stress orientation is needed to generate oblique faulting. We conclude that regional-stress orientation may be misleading when assessing propensity for failure; this has important implications for seismic hazard assessment. Also, overpressurized pore fluids, non-optimally oriented and dynamically weak faults and a close to critical local stress state play major roles for our dynamic rupture models of the Pohang earthquake. Such factors may be assessed when planning and conducting EGS-type experiments, explorations, and operations.

Our dynamic rupture simulations reveal dynamic triggering from the main fault plane to the secondary fault plane without direct rupture branching but via “rupture jumping”. The preferred two fault plane simulation compares well to regional observed data such as moment release and far-field seismic waveforms. The single fault plane model, on the other hand, is unable to reproduce the observed non-DC focal mechanisms and surface displacement distributions due to simplicity of the dynamic rupture process and a shallower dip angle, respectively. Dynamic fault interaction, amplified by rapid stress changes due to seismic waves reverberating between the two fault planes, are needed to reproduce observations of a strong CLVD component. However, two simultaneously breaking fault planes cannot fully explain the observed source complexity.

We demonstrate the maturity and feasibility of high-resolution 3D modeling of rupture dynamics and seismic wave propagation accounting for the complexity of EGS environments and

688 constrained by few observational parameters shedding light on the dynamics of induced and
689 triggered earthquakes. More sophisticated 3D models, fully coupling dynamic earthquake rupture
690 and seismic wave propagation with co-seismic and quasi-static fluid effects, such as poroelasticity,
691 thermal pressurization, pore pressure diffusion, and considering the geometric complexity of
692 networks of fractures and non-planar faults, may allow in future to capture the full physical
693 complexity of nucleation and dynamics of induced earthquakes.

694 In the near future, such physics-based approaches may be synergistically integrated with
695 near-field seismic monitoring before, during, and after EGS operation, thus complementing traffic
696 light systems for hazard and risk mitigation (Bommer et al., 2006; Mignan et al., 2015).

697

698 Data and resources

699 All regional waveforms used in this study were downloaded from Incorporated Research
700 Institutions for Seismology (IRIS; https://www.iris.edu (last accessed February 2020)) data
701 management system using FDSN client. PREM anisotropic 2 s can be downloaded in the IRIS
702 data services products (http://ds.iris.edu/ds/products/syngine/ (last accessed February 2020)). All
703 parameters used for the preferred Model 2F are available at
704 (https://drive.google.com/open?id=1nm3HZ_YOD-j8t_YatTFfs9prVKplEExj). The
705 supplemental for this article provides additional figures, a table, and a movie mentioned in the
706 article.

707

708 Acknowledgments

709 We thank Xing Li and Prof. Sigurjón Jónsson for the discussions regarding surface deformations
710 using InSAR. We also thank Prof. Guy Ouillon for providing us the raw code of ACLUD. We

711 acknowledge Dr. Seok Goo Song and Prof. Hoonyol Lee for sharing the processed InSAR images
712 and discussions about inversion parameters. Computing resources were provided by King
713 Abdullah University of Science and Technology, Thuwal, Saudi Arabia (KAUST, project k1219
714 and k1343 on Shaheen II). The work presented in this paper was supported by The KAUST grants
715 (FRAGEN, ORS-2017-CRG6 3389.02), URF/1/3389-01-01, and BAS/1339-01-01. J.A.L-C has
716 also received funding from the European Union's Horizon 2020 research and innovation
717 programme under the Marie Skłodowska-Curie grant agreement Nº 754446 and UGR Research
718 and Knowledge Transfer Found – Athenea3i; and by the Deutsche Forschungsgemeinschaft (DFG,
719 German Research Foundation) – Projektnummer (407141557). TU and A.-A.G acknowledge
720 additional support by the European Union's Horizon 2020 research and innovation program
721 (ChEESE, grant no. 823844) and the European Research Council (TEAR, ERC Starting grant no.
722 852992). Part of the analysis was implemented using ObsPy (Beyreuther et al., 2010). Figures
723 were prepared using Paraview (Ahrens et al., 2005), Generic Mapping Tools (Wessel et al., 2013)
724 and Matplotlib (Hunter, 2007)
725

726 # References

727 Ahrens, J., B. Geveci, and C. Law, 2005, ParaView: An end-user tool for large-data
728 visualization, in Visualization Handbook, Elsevier Inc., 717–731.

729 Andrews, D. J., 2005, Rupture dynamics with energy loss outside the slip zone, J. Geophys. Res.,
730 110, no. B1, B01307, doi: 10.1029/2004JB003191.

731 Anger, S. and A.-A Gabriel (2019). Dynamic earthquake rupture across complex 3D
732 fracture networks. S55E-0444 presented at 2019 Fall Meeting, AGU, San Francisco, CA, 9-

733 13 Dec.

734 Aochi, H., and R. Madariaga, 2003, The 1999 Izmit, Turkey, earthquake: Nonplanar fault
735 structure, dynamic rupture process, and strong ground motion, Bull. Seismol. Soc. Am., 93,
736 no. 3, 1249–1266, doi: 10.1785/0120020167.

737 Aochi, H., O. Scotti, and C. Berge-Thierry, 2005, Dynamic transfer of rupture across differently
738 oriented segments in a complex 3-D fault system, Geophys. Res. Lett., 32, no. 21, L21304,
739 doi: 10.1029/2005GL024158.

740 Bauer, A., Scheipl, F., Küchenhoff, H., and Gabriel, A.-A. (2018). An introduction to
741 semiparametric function-on-scalar regression. Statistical Modelling, 18(3–4), 346–364.
742 https://doi.org/10.1177/1471082X17748034.

743 Beyreuther, M., R. Barsch, L. Krischer, T. Megies, Y. Behr, and J. Wassermann, 2010, ObsPy: A
744 python toolbox for seismology, Seismol. Res. Lett., 81, no. 3, 530–533, doi:
745 10.1785/gssrl.81.3.530.

746 Bhat, H. S., M. Olives, R. Dmowska, and J. R. Rice, 2007, Role of fault branches in earthquake
747 rupture dynamics, J. Geophys. Res., 112, no. B11, B11309, doi: 10.1029/2007JB005027.

748 Boitz, N., A. Reshetnikov, and S. A. Shapiro, 2018, Visualizing effects of anisotropy on seismic
749 moments and their potency-tensor isotropic equivalent, Geophysics, 83, no. 3, C85–C97,
750 doi: 10.1190/geo2017-0442.1.

751 Bommer, J.J., Oates, S., Cepeda, J.M., Lindholm, C., Bird, J., Torres, R., Marroquín, G. and
752 Rivas, J., 2006. Control of hazard due to seismicity induced by a hot fractured rock

753 geothermal project. Engineering Geology, 83(4), pp.287-306.

754 Breuer, A., A. Heinecke, and M. Bader, 2016, Petascale Local Time Stepping for the ADER-DG
755 Finite Element Method, in Proceedings - 2016 IEEE 30th International Parallel and
756 Distributed Processing Symposium, IPDPS 2016, Institute of Electrical and Electronics
757 Engineers Inc., 854–863.

758 Breuer, A., A. Heinecke, S. Rettenberger, M. Bader, A.-A. Gabriel, and C. Pelties, 2014,
759 Sustained Petascale Performance of Seismic Simulations with SeisSol on SuperMUC, 1–18.

760 Bydlon, S. A., and E. M. Dunham, 2015, Rupture dynamics and ground motions from
761 earthquakes in 2-D heterogeneous media, Geophys. Res. Lett., 42, no. 6, 1701–1709, doi:
762 10.1002/2014GL062982.

763 Cappa, F., and J. Rutqvist, 2012, Seismic rupture and ground accelerations induced by CO 2
764 injection in the shallow crust, Geophys. J. Int., 190, no. 3, 1784–1789, doi: 10.1111/j.1365-
765 246X.2012.05606.x.

766 Chang, K. W., H. Yoon, Y. Kim, and M. Y. Lee, 2020, Operational and geological controls of
767 coupled poroelastic stressing and pore-pressure accumulation along faults: Induced
768 earthquakes in Pohang, South Korea, Sci. Rep., 10, no. 1, 2073, doi: 10.1038/s41598-020-
769 58881-z.

770 Cheng, Y., and X. Chen, 2018, Characteristics of seismicity inside and outside the salton sea
771 geothermal field, Bull. Seismol. Soc. Am., 108, no. 4, 1877–1888, doi:
772 10.1785/0120170311.

773 Choi, J. H. et al., 2019, Surface deformations and rupture processes associated with the 2017 Mw
774 5.4 Pohang, Korea, earthquake, Bull. Seismol. Soc. Am., 109, no. 2, 756–769, doi:
775 10.1785/0120180167.

776 Cornet, F.H., Bérard, T. and Bourouis, S., 2007. How close to failure is a granite rock mass at a 5
777 km depth?. International Journal of Rock Mechanics and Mining Sciences, 44(1), pp.47-66.

778 Cuenot, N., J. Charléty, L. Dorbath, and H. Haessler, 2006, Faulting mechanisms and stress
779 regime at the European HDR site of Soultz-sous-Forêts, France, Geothermics, 35, nos. 5–6,
780 561–575, doi: 10.1016/j.geothermics.2006.11.007.

781 Dieterich, J. H., K. B. Richards-Dinger, and K. A. Kroll, 2015, Modeling injection-induced
782 seismicity with the physics-based earthquake simulator RSQSim, Seismol. Res. Lett., 86,
783 no. 4, 1102–1109, doi: 10.1785/0220150057.

784 Duan, B., 2016, Spontaneous rupture on natural fractures and seismic radiation during hydraulic
785 fracturing treatments, Geophys. Res. Lett., 43, no. 14, 7451–7458, doi:
786 10.1002/2016GL069083.

787 Dumbser, M., and M. Käser, 2006, An arbitrary high-order discontinuous Galerkin method for
788 elastic waves on unstructured meshes - II. The three-dimensional isotropic case, Geophys. J.
789 Int., 167, no. 1, 319–336, doi: 10.1111/j.1365-246X.2006.03120.x.

790 Dunham, E. M., D. Belanger, L. Cong, and J. E. Kozdon, 2011a, Earthquake ruptures with
791 strongly rate-weakening friction and off-fault plasticity, part 1: Planar faults, Bull. Seismol.
792 Soc. Am., 101, no. 5, 2296–2307, doi: 10.1785/0120100075.

793 Dunham, E. M., D. Belanger, L. Cong, and J. E. Kozdon, 2011b, Earthquake ruptures with
794 strongly rate-weakening friction and off-fault plasticity, part 2: Nonplanar faults, Bull.
795 Seismol. Soc. Am., 101, no. 5, 2308–2322, doi: 10.1785/0120100076.

796 Ellsworth, W. L., D. Giardini, J. Townend, S. Ge, and T. Shimamoto, 2019, Triggering of the
797 Pohang, Korea, Earthquake (Mw 5.5) by enhanced geothermal system stimulation,
798 Seismological Society of America, 1844–1858.

799 Emerson paradigm holding, 2018, GoCad: A computer aided design program for geological
800 applications.

801 Gabriel, A.-A., J.-P. Ampuero, L. A. Dalguer, and P. M. Mai, 2013, Source properties of
802 dynamic rupture pulses with off-fault plasticity, J. Geophys. Res. Solid Earth, 118, no. 8,
803 4117–4126, doi: 10.1002/jgrb.50213.

804 Galis, M., J. P. Ampuero, P. M. Mai, and F. Cappa, 2017, Induced seismicity provides insight
805 into why earthquake ruptures stop, Sci. Adv., 3, no. 12, doi: 10.1126/sciadv.aap7528.

806 Gallovič, F., Valentová, Ľ., Ampuero, J.-P., and Gabriel, A.-A. , 2019a. Bayesian dynamic finite-
807 fault inversion: 1. Method and synthetic test. J. Geophys. Res., 124, 6949– 6969.
808 https://doi.org/10.1029/2019JB017510

809 Gallovič, F., Valentová, Ľ., Ampuero, J.-P., and Gabriel, A.-A., 2019b. Bayesian Dynamic
810 Finite-Fault Inversion: 2. Application to the 2016 Mw6.2 Amatrice, Italy, Earthquake, J.
811 Geophys. Res., doi:10.1029/2019JB017512.

812 Garagash, D. I., and L. N. Germanovich, 2012, Nucleation and arrest of dynamic slip on a

pressurized fault, J. Geophys. Res. B Solid Earth, 117, no. 10, doi: 10.1029/2012JB009209.

Grigoli, F., S. Cesca, A. P. Rinaldi, A. Manconi, J. A. López-Comino, J. F. Clinton, R. Westaway, C. Cauzzi, T. Dahm, and S. Wiemer, 2018, The November 2017 M w 5.5 Pohang earthquake: A possible case of induced seismicity in South Korea, Science (80-.)., 360, no. 6392, 1003–1006, doi: 10.1126/science.aat2010.

Happ, C., Scheipl, F., Gabriel, A.-A., Greven, S. A general framework for multivariate functional principal component analysis of amplitude and phase variation. Stat. 2019; 8:e220. https://doi.org/10.1002/sta4.220

Hardebeck, J. L., and A. J. Michael, 2006, Damped regional-scale stress inversions: Methodology and examples for southern California and the Coalinga aftershock sequence, J. Geophys. Res. Solid Earth, 111, no. B11, doi: 10.1029/2005JB004144.

Harris, R. A. et al., 2018, A suite of exercises for verifying dynamic earthquake rupture codes, Seismol. Res. Lett., 89, no. 3, 1146–1162, doi: 10.1785/0220170222.

Harris, R. A. et al., 2011, Verifying a Computational Method for Predicting Extreme Ground Motion, Seismol. Res. Lett., 82, no. 5, 638–644, doi: 10.1785/gssrl.82.5.638.

Heidbach, O. M. Rajabi, X. Cui, K. Fuchs, B. Muller, J. Reinecker, K. Reiter, M. Tingay, F. Wenzel, F. Xie, M. O. Ziegler, M.-L Zoback, M. Zoback, 2018, The World Stress Map database release 2016: Crustal stress pattern across scales, Elsevier B.V., 484–498.

Heinecke, A., A. Breuer, S. Retenberger, M. Bader, A.-A. Gabriel, C. Pelties, A. Bode, W. Barth, X. Liao, K. Vaidyanathan, M. Smelyankiy, P. Dubei, 2014, Petascale High Order

833 Dynamic Rupture Earthquake Simulations on Heterogeneous Supercomputers, in
834 International Conference for High Performance Computing, Networking, Storage and
835 Analysis, SC, IEEE Computer Society, 3–14.

836 Hirata, T., 1989, Fractal dimension of fault systems in Japan: Fractal structure in rock fracture
837 geometry at various scales, Pure Appl. Geophys. PAGEOPH, 131, nos. 1–2, 157–170, doi:
838 10.1007/BF00874485.

839 Hofmann, H., G, Zimmermann,M. Farkas, E. Huenges, A. Zang, M. Leonhardt et al., 2019, First
840 field application of cyclic soft stimulation at the Pohang Enhanced Geothermal System site
841 in Korea, Geophys. J. Int. (2019) 217, 926–949

842 Hunter, J. D., 2007, Matplotlib: A 2D graphics environment, Comput. Sci. Eng., 9, no. 3, 99–
843 104, doi: 10.1109/MCSE.2007.55.

844 Jeanne, P., J. Rutqvist, P. F. Dobson, J. Garcia, M. Walters, C. Hartline, and A. Borgia, 2015,
845 Geomechanical simulation of the stress tensor rotation caused by injection of cold water in a
846 deep geothermal reservoir, J. Geophys. Res. Solid Earth, 120, no. 12, 8422–8438, doi:
847 10.1002/2015JB012414.

848 Jin, L., and M. D. Zoback, 2018, Fully Dynamic Spontaneous Rupture Due to Quasi-Static Pore
849 Pressure and Poroelastic Effects: An Implicit Nonlinear Computational Model of Fluid-
850 Induced Seismic Events, J. Geophys. Res. Solid Earth, 123, no. 11, 9430–9468, doi:
851 10.1029/2018JB015669.

852 Julian, B. R., A. D. Miller, and G. R. Foulger, 1998, Non-double-couple earthquakes 1. Theory,
853 Rev. Geophys., 36, no. 4, 525–549, doi: 10.1029/98RG00716.

Kang, S., B. Kim, S. Bae, H. Lee, and M. Kim, 2019a, Earthquake-Induced Ground Deformations in the Low-Seismicity Region: A Case of the 2017 M5.4 Pohang, South Korea, Earthquake, Earthq. Spectra, 35, no. 3, 1235–1260, doi: 10.1193/062318EQS160M.

Kang, S., B. Kim, H. Cho, J. Lee, K. Kim, S. Bae, and C. Sun, 2019b, Ground-Motion Amplifications in Small-Size Hills: Case Study of Gokgang-ri, South Korea, during the 2017 ML 5.4 Pohang Earthquake Sequence, Bull. Seismol. Soc. Am., 109, no. 6, 2626–2643, doi: 10.1785/0120190064.

Käser, M., and M. Dumbser, 2006, An arbitrary high-order discontinuous Galerkin method for elastic waves on unstructured meshes - I. The two-dimensional isotropic case with external source terms, Geophys. J. Int., 166, no. 2, 855–877, doi: 10.1111/j.1365-246X.2006.03051.x.

Kim, K. H., J. H. Ree, Y. H. Kim, S. Kim, S. Y. Kang, and W. Seo, 2018, Assessing whether the 2017 Mw5.4 Pohang earthquake in South Korea was an induced event, Science (80-.)., 360, no. 6392, 1007–1009, doi: 10.1126/science.aat6081.

Kim, K. H., W. Seo, J. Han, J. Kwon, S. Y. Kang, J. H. Ree, S. Kim, and K. Liu, 2020, The 2017 ML 5.4 Pohang earthquake sequence, Korea, recorded by a dense seismic network, Tectonophysics, 774, doi: 10.1016/j.tecto.2019.228306.

Kim, H., L. Xie, K. B. Min, S. Bae, and O. Stephansson, 2017, Integrated In Situ Stress Estimation by Hydraulic Fracturing, Borehole Observations and Numerical Analysis at the EXP-1 Borehole in Pohang, Korea, Rock Mech. Rock Eng., 50, no. 12, 3141–3155, doi: 10.1007/s00603-017-1284-1.

875 Klinger, Y., K. Okubo, A. Vallage, J. Champenois, A. Delorme, E. Rougier, Z. Lei, E. E. Knight,
876 A. Munjiza, C. Satriano, S. Baize, R. Langridge, H. S. Bhat, 2018, Earthquake Damage
877 Patterns Resolve Complex Rupture Processes, Geophys. Res. Lett., 45, no. 19, 10,279-
878 10,287, doi: 10.1029/2018GL078842.

879 Korean Government Commission, 2019, Summary Report of the Korean Government
880 Commission on Relations between the 2017 Pohang Earthquake and EGS Project.

881 Krischer, L., A. R. Hutko, M. Van Driel, S. Stähler, M. Bahavar, C. Trabant, and T. Nissen-
882 Meyer, 2017, On-demand custom broadband synthetic seismograms, Seismol. Res. Lett.,
883 88, no. 4, 1127–1140, doi: 10.1785/0220160210.

884 Kroll, K. A., K. B. Richards-Dinger, and J. H. Dieterich, 2017, Sensitivity of Induced Seismic
885 Sequences to Rate-and-State Frictional Processes, J. Geophys. Res. Solid Earth, 122, no. 12,
886 10,207-10,219, doi: 10.1002/2017JB014841.

887 Kwiatek, G. et al., 2019, Controlling fluid-induced seismicity during a 6.1-km-deep geothermal
888 stimulation in Finland, Sci. Adv., 5, no. 5, eaav7224, doi: 10.1126/sciadv.aav7224.

889 Kyriakopoulos, C., D. D. Oglesby, T. K. Rockwell, A. J. Meltzner, M. Barall, J. M. Fletcher, and
890 D. Tulanowski, 2019, Dynamic Rupture Scenarios in the Brawley Seismic Zone, Salton
891 Trough, Southern California, J. Geophys. Res. Solid Earth, 124, no. 4, 3680–3707, doi:
892 10.1029/2018JB016795.

893 de la Puente, J., J.-P. Ampuero, and M. Käser, 2009, Dynamic rupture modeling on unstructured
894 meshes using a discontinuous Galerkin method, J. Geophys. Res., 114, no. B10, B10302,
895 doi: 10.1029/2008JB006271.

Lee, K. K. et al., 2019, Managing injection-induced seismic risks, Science, 364, no. 6442, 730–732, doi: 10.1126/science.aax1878.

Lee, J., T. K. Hong, and C. Chang, 2017, Crustal stress field perturbations in the continental margin around the Korean Peninsula and Japanese islands, Tectonophysics, 718, 140–149, doi: 10.1016/j.tecto.2017.08.003.

Lee, H., Y. J. Shinn, S. H. Ong, S. W. Woo, K. G. Park, T. J. Lee, and S. W. Moon, 2017, Fault reactivation potential of an offshore CO2 storage site, Pohang Basin, South Korea, J. Pet. Sci. Eng., 152, 427–442, doi: 10.1016/j.petrol.2017.03.014.

Liu, J. and Zahradník, J., The 2019 MW 5.7 Changning earthquake, Sichuan Basin, China–a shallow doublet with different faulting styles. Geophys. Res. Let., p.e2019GL085408.

Ma, S., 2008, A physical model for widespread near-surface and fault zone damage induced by earthquakes. *Geochemistry, Geophysics, Geosystems*, *9*(11).

Mai, P. M., M. Galis, K. K. S. Thingbaijam, J. C. Vyas, and E. M. Dunham, 2018, Accounting for Fault Roughness in Pseudo-Dynamic Ground-Motion Simulations, Birkhäuser, Cham, 95–126.

Martínez-Garzón, P., M. Bohnhoff, G. Kwiatek, and G. Dresen, 2013, Stress tensor changes related to fluid injection at The Geysers geothermal field, California, Geophys. Res. Lett., 40, no. 11, 2596–2601, doi: 10.1002/grl.50438.

Martínez-Garzón, P., G. Kwiatek, H. Sone, M. Bohnhoff, G. Dresen, and C. Hartline, 2014, Spatiotemporal changes, faulting regimes, and source parameters of induced seismicity: A

916 case study from The Geysers geothermal field, J. Geophys. Res. Solid Earth, 119, no. 11,
917 8378–8396, doi: 10.1002/2014JB011385.

918 McGarr, A., 2014, Maximum magnitude earthquakes induced by fluid injection, J. Geophys.
919 Res. Solid Earth, 119, no. 2, 1008–1019, doi: 10.1002/2013JB010597.

920 Mignan, A., Landtwing, D., Kästli, P., Mena, B. and Wiemer, S., 2015. Induced seismicity risk
921 analysis of the 2006 Basel, Switzerland, Enhanced Geothermal System project: Influence of
922 uncertainties on risk mitigation. *Geothermics*, *53*, pp.133-146.

923 Okubo, K., H. S. Bhat, E. Rougier, S. Marty, A. Schubnel, Z. Lei, E. E. Knight, and Y. Klinger,
924 2019, Dynamics, Radiation, and Overall Energy Budget of Earthquake Rupture With
925 Coseismic Off-Fault Damage, J. Geophys. Res. Solid Earth, 124, no. 11, 11771–11801, doi:
926 10.1029/2019JB017304.

927 Pelties, C., A.-A. Gabriel, and J.-P. Ampuero, 2014, Verification of an ADER-DG method for
928 complex dynamic rupture problems, Geosci. Model Dev., 7, no. 3, 847–866, doi:
929 10.5194/gmd-7-847-2014 and Geoscientific Model Development Discussions, 6(4), 5981--
930 6034, doi:10.5194/gmdd-6-5981-2013.

931 Pelties, C., Y. Huang, and J. P. Ampuero, 2015, Pulse-Like Rupture Induced by Three-
932 Dimensional Fault Zone Flower Structures, Pure Appl. Geophys., 172, no. 5, 1229–1241,
933 doi: 10.1007/s00024-014-0881-0.

934 Pelties, C., J. de la Puente, J.-P. Ampuero, G. B. Brietzke, and M. Käser, 2012, Three-
935 dimensional dynamic rupture simulation with a high-order discontinuous Galerkin method
936 on unstructured tetrahedral meshes, J. Geophys. Res. Solid Earth, 117, no. B2, n/a-n/a, doi:

10.1029/2011JB008857.

Peyrat, S., K. Olsen, and R. Madariaga, 2001, Dynamic modeling of the 1992 Landers earthquake, J. Geophys. Res. Solid Earth, 106, no. B11, 26467–26482, doi: 10.1029/2001jb000205.

Rettenberger, S., O. Meister, M. Bader, and A. A. Gabriely, 2016, ASAGI - A parallel server for adaptive geoinformation, in ACM International Conference Proceeding Series, Association for Computing Machinery.

Richards-Dinger, K., and J. H. Dieterich, 2012, RSQSim earthquake simulator, Seismol. Res. Lett., 83, no. 6, 983–990, doi: 10.1785/0220120105.

Ripperger, J., Mai, P.M. and Ampuero, J.P., 2008. Variability of near-field ground motion from dynamic earthquake rupture simulations. *Bulletin of the seismological society of America*, *98*(3), pp.1207-1228.

Roten, D., K. B. Olsen, S. M. Day, Y. Cui, and D. Fäh, 2014, Expected seismic shaking in Los Angeles reduced by San Andreas fault zone plasticity, Geophys. Res. Lett., 41, no. 8, 2769–2777, doi: 10.1002/2014GL059411.

Schoenball, M., L. Dorbath, E. Gaucher, J. F. Wellmann, and T. Kohl, 2014, Change of stress regime during geothermal reservoir stimulation, Geophys. Res. Lett., 41, no. 4, 1163–1170, doi: 10.1002/2013GL058514.

Schoenball, M., T. M. Müller, B. I. R. Müller, and O. Heidbach, 2010, Fluid-induced microseismicity in pre-stressed rock masses, Geophys. J. Int., 180, no. 2, 813–819, doi:

957 10.1111/j.1365-246X.2009.04443.x.

958 Shi, Z., and S. M. Day, 2013, Rupture dynamics and ground motion from 3-D rough-fault
959 simulations, J. Geophys. Res. Solid Earth, 118, no. 3, 1122–1141, doi: 10.1002/jgrb.50094.

960 Simmetrix Inc, 2017, SimModeler: Simulation modeling suite 14.0 documentation (Tech. Rep.).

961 Soh, I., C. Chang, J. Lee, T.-K. Hong, and E.-S. Park, 2018, Tectonic stress orientations and
962 magnitudes, and friction of faults, deduced from earthquake focal mechanism inversions
963 over the Korean Peninsula, Geophys. J. Int., 213, no. 2, 1360–1373, doi:
964 10.1093/gji/ggy061.

965 Song, S. G., and H. Lee, 2019, Static slip model of the 2017 M w 5.4 Pohang, South Korea,
966 earthquake constrained by the InSAR data, Seismol. Res. Lett., 90, no. 1, 140–148, doi:
967 10.1785/0220180156.

968 Di Toro, G., R. Han, T. Hirose, N. De Paola, S. Nielsen, K. Mizoguchi, F. Ferri, M. Cocco, and
969 T. Shimamoto, 2011, Fault lubrication during earthquakes, Nature, 471, no. 7339, 494–499,
970 doi: 10.1038/nature09838.

971 Taufiqurrahman, T., A.-A. Gabriel, B. Li, D. Li, S. A. Wirp, T. Ulrich, K. H. Palgunadi, A.
972 Verdecchia, S. Carena, and Z. K. Mildon, 2019, High-resolution integrated dynamic rupture
973 modeling of the 2019 M6. 4 Searles Valley and M7. 1 Ridgecrest earthquakes. S31G-0487
974 presented at 2019 Fall Meeting, AGU, San Francisco, CA, 9-13 Dec.

975 Templeton, E.L. and Rice, J.R., 2008. Off-fault plasticity and earthquake rupture dynamics: 1.
976 Dry materials or neglect of fluid pressure changes. J. Geophys. Res.: Solid Earth, 113(B9).

977 Ulrich, T., and A.-A. Gabriel, 2017, 3D fault curvature and fractal roughness: Insights for
978 rupture dynamics and ground motions using a Discontinuous Galerkin method. In EGU
979 General Assembly Conference Abstract, Vol. 19, Vienna, Austria, pp. 18689.

980 Ulrich, Thomas, A. A. Gabriel, J. P. Ampuero, and W. Xu, 2019a, Dynamic viability of the 2016
981 Mw 7.8 Kaikōura earthquake cascade on weak crustal faults, Nat. Commun., 10, no. 1, doi:
982 10.1038/s41467-019-09125-w.

983 Ulrich, T., S. Vater, E. H. Madden, J. Behrens, Y. van Dinther, I. van Zelst, E. J. Fielding, C.
984 Liang, and A. A. Gabriel, 2019b, Coupled, Physics-Based Modeling Reveals Earthquake
985 Displacements are Critical to the 2018 Palu, Sulawesi Tsunami, Pure Appl. Geophys., 176,
986 no. 10, 4069–4109, doi: 10.1007/s00024-019-02290-5.

987 Uphoff, C. and Bader, M., 2016, July. Generating high performance matrix kernels for
988 earthquake simulations with viscoelastic attenuation. In 2016 International Conference on
989 High Performance Computing and Simulation (HPCS) (pp. 908-916). IEEE.

990 Uphoff, C., S. Rettenberger, M. Bader, E. H. Madden, T. Ulrich, S. Wollherr, and A.-A. Gabriel,
991 2017, Extreme scale multi-physics simulations of the tsunamigenic 2004 sumatra
992 megathrust earthquake, Proc. Int. Conf. High Perform. Comput. Networking, Storage Anal.
993 - SC '17, no. November, 1–16, doi: 10.1145/3126908.3126948.

994 Vavryčuk, V., 2015, Moment tensor decompositions revisited, J. Seismol., 19, no. 1, 231–252,
995 doi: 10.1007/s10950-014-9463-y.

996 Viesca, R. C., and J. R. Rice, 2012, Nucleation of slip-weakening rupture instability in landslides
997 by localized increase of pore pressure, J. Geophys. Res. Solid Earth, 117, no. 3, doi:

998 10.1029/2011JB008866.

999 Wang, Y., G. Ouillon, J. Woessner, D. Sornette, and S. Husen, 2013, Automatic reconstruction
1000 of fault networks from seismicity catalogs including location uncertainty, J. Geophys. Res.
1001 Solid Earth, 118, no. 11, 5956–5975, doi: 10.1002/2013JB010164.

1002 Wessel, P., W. H. F. Smith, R. Scharroo, J. Luis, and F. Wobbe, 2013, Generic Mapping Tools:
1003 Improved Version Released, Eos, Trans. Am. Geophys. Union, 94, no. 45, 409–410, doi:
1004 10.1002/2013EO450001.

1005 Wolf, Sebastian, A.-A. Gabriel, and M. Bader (2020), Optimisation and Local Time Stepping of
1006 an ADER-DG Scheme for Fully Anisotropic Wave Propagation in Complex Geometries, in
1007 Proceedings of the 10th International Workshop on Advances in High-Performance
1008 Computational Earth Sciences: Applications and Frameworks, preprint available at
1009 https://wolke.geophysik.uni-muenchen.de/s/ReaBg7mjabPwwLk#pdfviewer.

1010 Wollherr, S., A. Gabriel, and P. M. Mai, 2019, Landers 1992 “Reloaded”: Integrative Dynamic
1011 Earthquake Rupture Modeling, J. Geophys. Res. Solid Earth, 124, no. 7, 6666–6702, doi:
1012 10.1029/2018JB016355.

1013 Wollherr, S., A. A. Gabriel, and C. Uphoff, 2018, Off-fault plasticity in three-dimensional
1014 dynamic rupture simulations using a modal Discontinuous Galerkin method on unstructured
1015 meshes: Implementation, verification and application, Geophys. J. Int., 214, no. 3, 1556–
1016 1584, doi: 10.1093/GJI/GGY213.

1017 Woo, J. -U., M. Kim, D. -H. Sheen, T. -S. Kang, J. Rhie, F. Grigoli, W. L. Ellsworth, and D.
1018 Giardini, 2019, An In-Depth Seismological Analysis Revealing a Causal Link Between the

2017 M w 5.5 Pohang Earthquake and EGS Project, J. Geophys. Res. Solid Earth, 2019JB018368, doi: 10.1029/2019JB018368.

Yamashita, T., and Y. Umeda, 1994, Earthquake rupture complexity due to dynamic nucleation and interaction of subsidiary faults, Pure Appl. Geophys. PAGEOPH, 143, nos. 1–3, 89–116, doi: 10.1007/BF00874325.

Zaliapin, I., and Y. Ben-Zion, 2013, Earthquake clusters in southern California I: Identification and stability, J. Geophys. Res. Solid Earth, 118, no. 6, 2847–2864, doi: 10.1002/jgrb.50179.

van Zelst, I., S. Wollherr, A. -A. Gabriel, E. H. Madden, and Y. Dinther, 2019, Modeling Megathrust Earthquakes Across Scales: One-way Coupling From Geodynamics and Seismic Cycles to Dynamic Rupture, J. Geophys. Res. Solid Earth, 124, no. 11, 11414–11446, doi: 10.1029/2019JB017539.

Zhan, Z., 2019, Distributed acoustic sensing turns fiber-optic cables into sensitive seismic antennas, Seismol. Res. Lett., 91, no. 1, 1–15, doi: 10.1785/0220190112.

Zhang, Q., and P. M. Shearer, 2016, A new method to identify earthquake swarms applied to seismicity near the San Jacinto Fault, California, Geophys. J. Int., 205, no. 2, 995–1005, doi: 10.1093/gji/ggw073.

Ziegler, M. O., O. Heidbach, A. Zang, P. Martínez-Garzón, and M. Bohnhoff, 2017, Estimation of the differential stress from the stress rotation angle in low permeable rock, Geophys. Res. Lett., 44, no. 13, 6761–6770, doi: 10.1002/2017GL073598.

FULL AUTHOR'S MAILING LIST

Kadek Hendrawan Palgunadi : kadek.palgunadi@kaust.edu.sa

Alice-Agnes Gabriel : gabriel@geophysik.uni-muenchen.de

Thomas Ulrich : ulrich@geophysik.uni-muenchen.de

José Ángel Lopéz-Comino : lopezcomino@uni-potsdam.de

Paul Martin Mai : martin.mai@kaust.edu.sa

TABLES:

Table 1. *Fault friction parameters assumed in this study*

Parameter	Symbol	Value
Direct effect parameter	a	0.01 - 0.02 for z≤3.3 km and 0.01 for z > 3.3 km
Evolution effect parameter	b	0.014
Reference slip velocity	V_0	10^{-6}m/s
Steady-state friction coefficient at V_0	f_0	0.6
State-evolution distance	L	0.2 m
Weakening slip velocity	V_W	0.1 - 1.0 for z≤3.3 km and 0.1 for z > 3.3 km
Fully weakened friction coefficient	f_W	0.1
Initial slip rate	V_{ini}	10^{-16}m/s

LIST OF FIGURE CAPTIONS:

Figure 1. Map of the South Korean Peninsula showing the near-regional broadband stations (blue triangles). Solid and dashed lines represent the Yangsan and interpreted geological faults near the Pohang EGS site, respectively. The two inset plots present the location and geometry of the faults of Model 1F (upper panel) and Model 2F (lower panel). The thicker black lines mark the near-surface edge of the fault planes. Colored dots depict aftershocks locations extracted from Kim et al. (2018). The non-double-couple solution of Grigoli et al. (2018) is also shown.

Figure 2. Fault reconstruction using guided anisotropic location uncertainty distribution (g-ACLUD). a) Spatiotemporal density plot of the mainshock and aftershocks based on the nearest-neighbor distance. b), c) and d) Two fault plane geometry inferred by the g-ACLUD method. The main fault plane has a strike of 214° and dips at 65°, while the secondary fault plane has a strike 199° and dips at 60°. Black dots depict the seismicity used in this study. The geometry of the faults is shown in views b) as view from North, in c) as view from South, and d) in map view. The red star denotes the hypocenter of the Pohang earthquake.

Figure 3. 3D rendering of the unstructured tetrahedral computational mesh, and the fault plane with final slip on the 2 fault preferred model (Model 2F) of the Pohang earthquake (warm colors, in m), and the radiated seismic wavefield 5 seconds after rupture initiation (cold colors, absolute particle velocity in m/s). Note the strong effect of the high-resolution topography on modulating the seismic wavefield.

Figure 4. Graphical summary of the outcome of 180 dynamic rupture simulations assuming different combinations of initial relative prestress ratio (R_0), fluid-pressure ratio (γ) and direction of S_{Hmax}. The corresponding 180 square frames are filled with color if the combination of parameters is able to trigger self-sustained rupture beyond the nucleation region on any fault. The S_{Hmax} direction is indicated by the size of the frame, leading to six imbricated frames for each set of prestress and fluid-pressure ratio parameters.

Figure 5. Overview of the simulated earthquake rupture of the preferred model (Model 2F), showing in a) and b) the space-time evolutions of the absolute slip-rate (in m/s) across the main and secondary fault plane. a) (left panel) view from North displaying the main fault rupture. Snapshots every 0.1 s. (right panel) view from South highlighting the rupture of a portion of the secondary fault. Snapshots every 0.05 s. b-c) Rupture-time contours at intervals of 0.2 s.

Figure 6. Distribution of absolute fault slip (in m) in a) and b), and rake angles (in degrees) in c) and d) for the preferred dynamic rupture scenario (Model 2F) a) and c) view from North highlighting the main fault rupture. b) and d) view from South highlighting the rupture of a portion of the secondary fault. The white star in panel a) marks the considered hypocenter location.

Figure 7. Moment rate release of a) Model 1F and b) Model 2F and moment tensor representation of the preferred one-fault c) and two-fault d) models.

Figure 8. Comparison of synthetic and observed ground motion waveforms. a) Distribution of virtual stations (green triangles) at which synthetic waveforms are compared in b). The beachball

is the moment tensor representation of the preferred 2 planes model scenario (Model 2F). Solid and dashed red lines represent the mapped Yangsan fault surface trace and the interpreted fault traces near the Pohang EGS site, respectively. The two rectangles show the location and geometry of the faults used in this study. b) Comparison of synthetic waveforms using one (Model 1F, blue dashed lines) and two fault planes (Model 2F, red solid lines) at the 19 dummy stations located in a). A 0.1 - 2 Hz 4^{th}order Butterworth filter is applied to all traces. All traces are normalized. For each trace, the maximum velocity amplitude (in m/s) of Model 1F is indicated within a black square. c) Observed (black) and synthetic (red) waveforms for five regional stations for up-down (UD), east-west (EW) and north-south (NS) components (all located in South Korea, see blue triangles in Figure 1. t = 0 s denotes the origin time of the Pohang earthquake. A 0.033-0.08 Hz 4^{th} order Butterworth filter is applied to all traces. Synthetic regional waveforms are generated from the preferred dynamic rupture scenario Model 2F using Instaseis (Krischer et al., 2017) and 2 s accurate Green's functions based on the PREM anisotropic model.

Figure 9. ((a) and (b)) Co-seismic surface displacements in the InSAR Line-of-sight (LoS) direction (in m) generated by a) Model 1F; one-plane (rectangle) and b) Model 2F; two-planes (two rectangles) preferred dynamic rupture scenario, respectively. The dashed red lines represent the traces of the interpreted faults near the EGS site.

FIGURES:

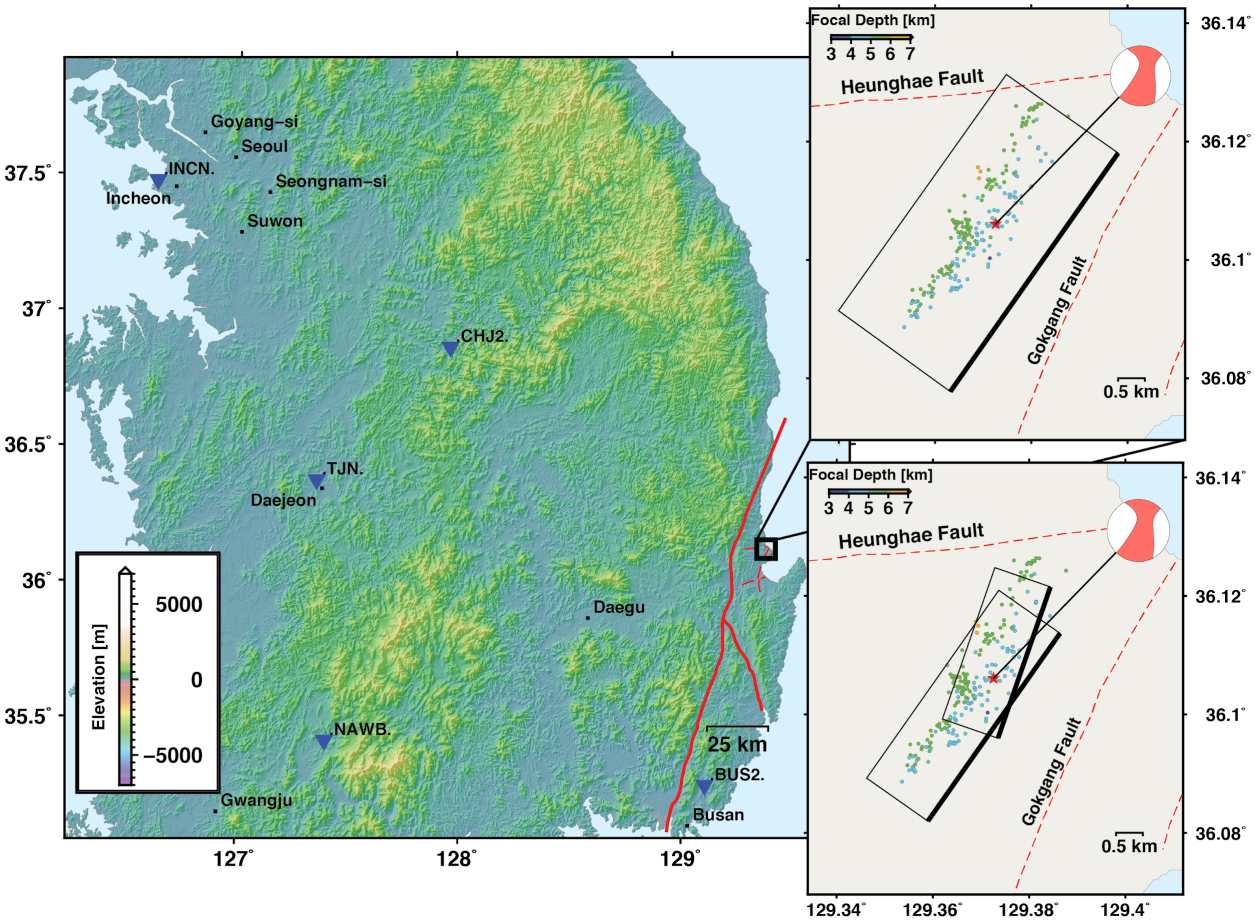

1115

1116 **Figure 1.** Map of the South Korean Peninsula showing the near-regional broadband stations (blue

1117 triangles). Solid and dashed lines represent the Yangsan and interpreted geological faults near the

1118 Pohang EGS site, respectively. The two inset plots present the location and geometry of the faults

1119 of Model 1F (upper panel) and Model 2F (lower panel). The thicker black lines mark the near-

1120 surface edge of the fault planes. Colored dots depict aftershocks locations extracted from Kim et

1121 al. (2018). The non-double-couple solution of Grigoli et al. (2018) is also shown.

1122

1123

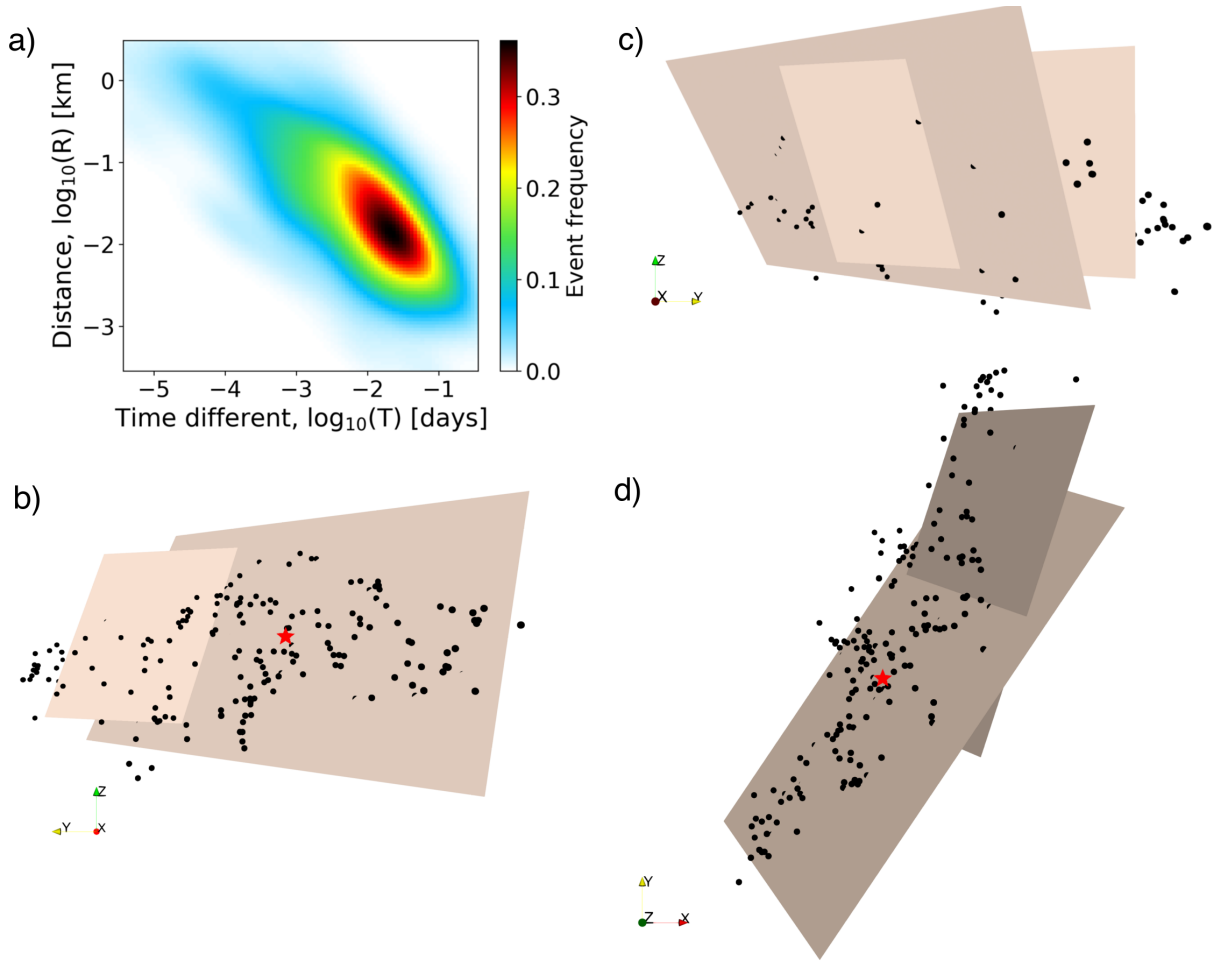

Figure 2. Fault reconstruction using guided anisotropic location uncertainty distribution (g-ACLUD). a) Spatiotemporal density plot of the mainshock and aftershocks based on the nearest-neighbor distance. b), c) and d) Two fault plane geometry inferred by the g-ACLUD method. The main fault plane has a strike of 214° and dips at 65°, while the secondary fault plane has a strike 199° and dips at 60°. Black dots depict the seismicity used in this study. The geometry of the faults is shown in views b) as view from North, in c) as view from South, and d) in map view. The red star denotes the hypocenter of the Pohang earthquake.

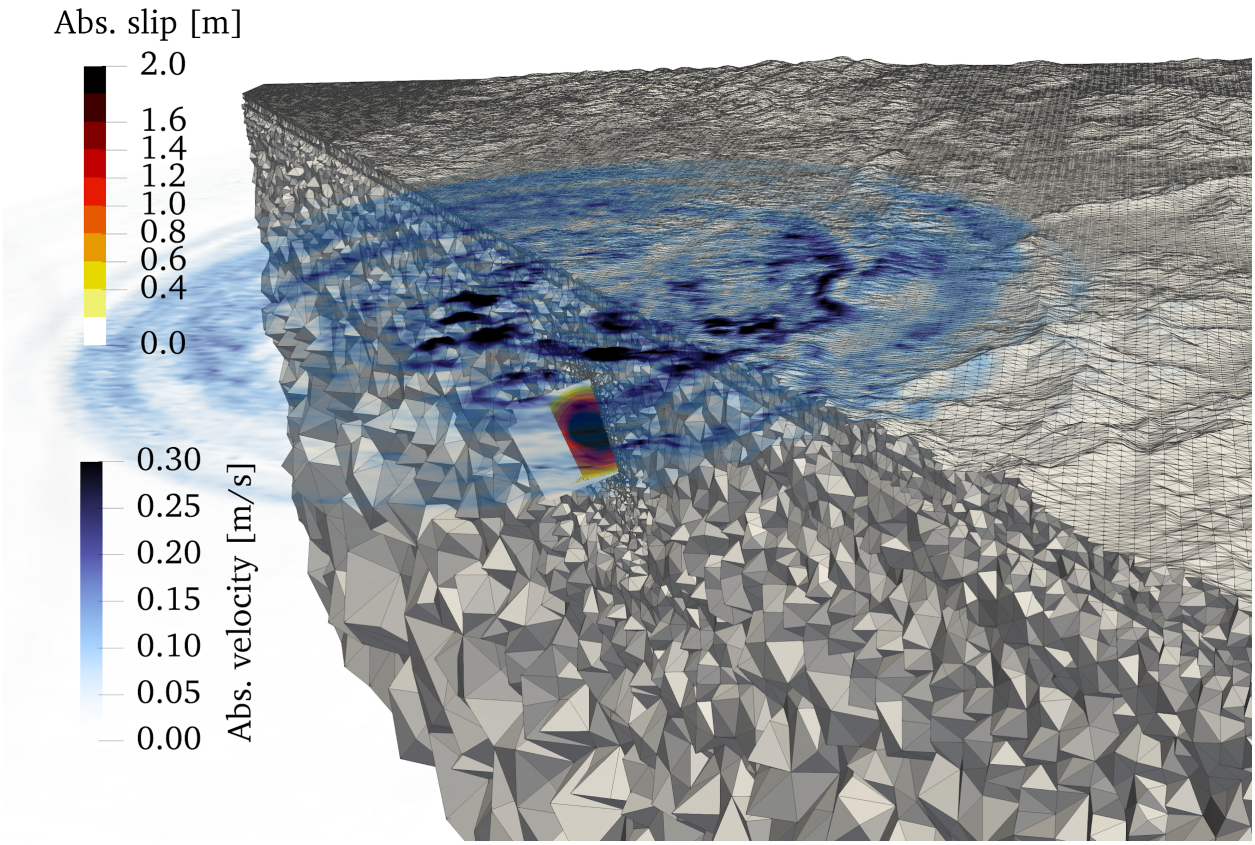

Figure 3. 3D rendering of the unstructured tetrahedral computational mesh, and the fault plane with final slip on the 2-fault preferred model (Model 2F) of the Pohang earthquake (warm colors, in m), and the radiated seismic wavefield 5 seconds after rupture initiation (cold colors, absolute particle velocity in m/s). Note the strong effect of the high-resolution topography on modulating the seismic wavefield.

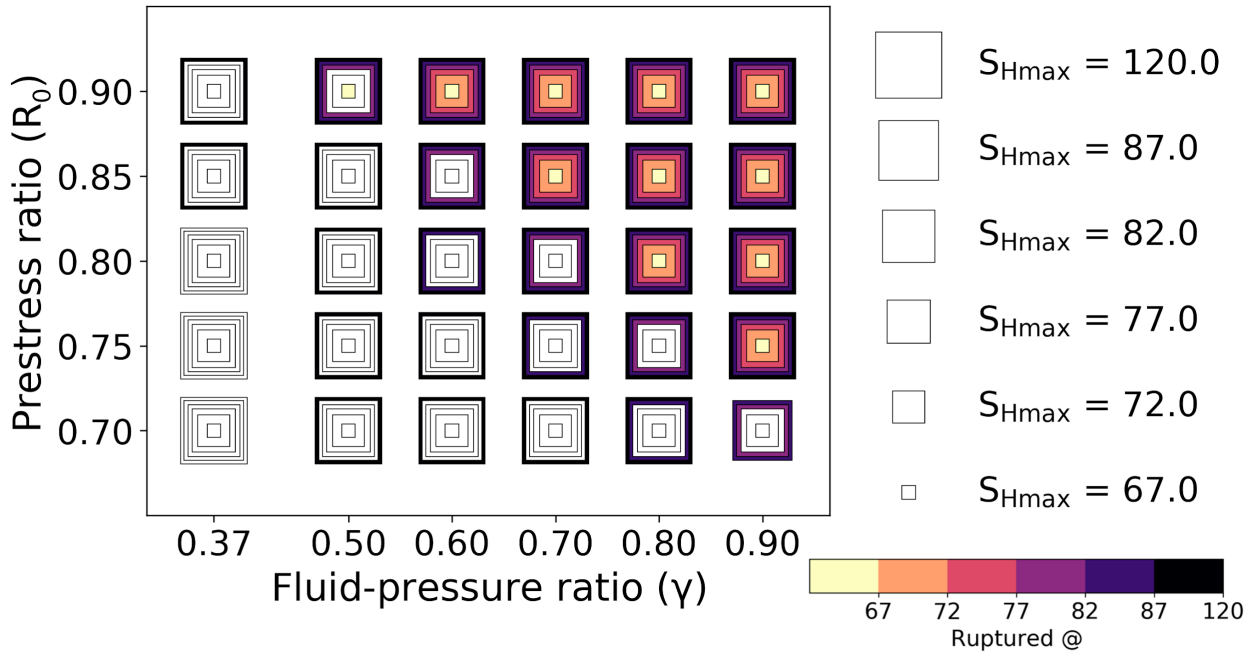

Figure 4. Graphical summary of the outcome of 180 dynamic rupture simulations assuming different combinations of initial relative prestress ratio (R_0), fluid-pressure ratio (γ) and direction of S_{Hmax}. The corresponding 180 square frames are filled with color if the combination of parameters is able to trigger self-sustained rupture beyond the nucleation region on any fault. The S_{Hmax} direction is indicated by the size of the frame, leading to six imbricated frames for each set of prestress and fluid-pressure ratio parameters.

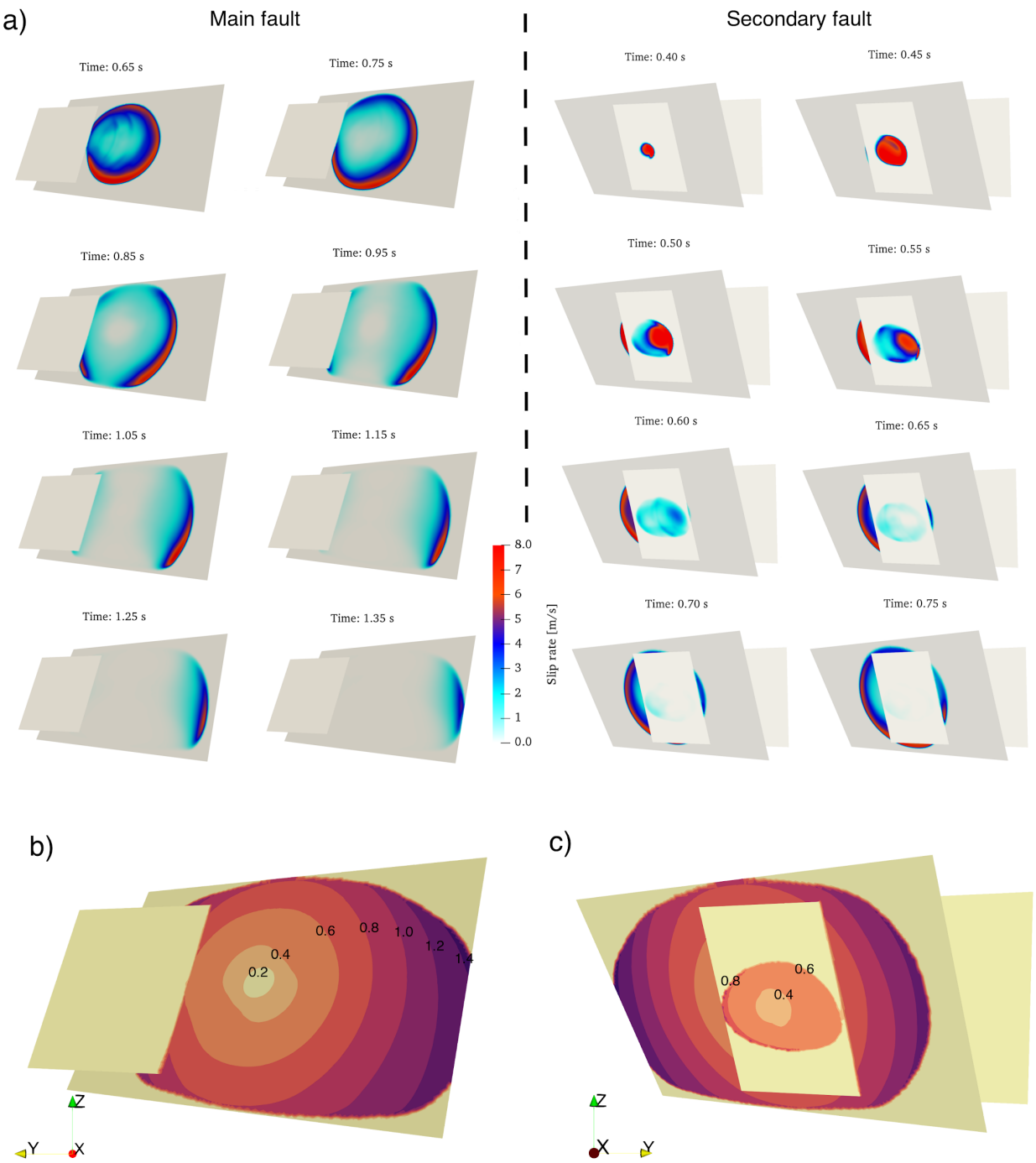

Figure 5. Overview of the simulated earthquake rupture of the preferred model (Model 2F), showing in a) and b) the space-time evolutions of the absolute slip-rate (in m/s) across the main and secondary fault plane. a) (left panel) view from North displaying the main fault rupture.

Snapshots every 0.1 s. (right panel) view from South highlighting the rupture of a portion of the secondary fault. Snapshots every 0.05 s. b-c) Rupture-time contours at intervals of 0.2 s.

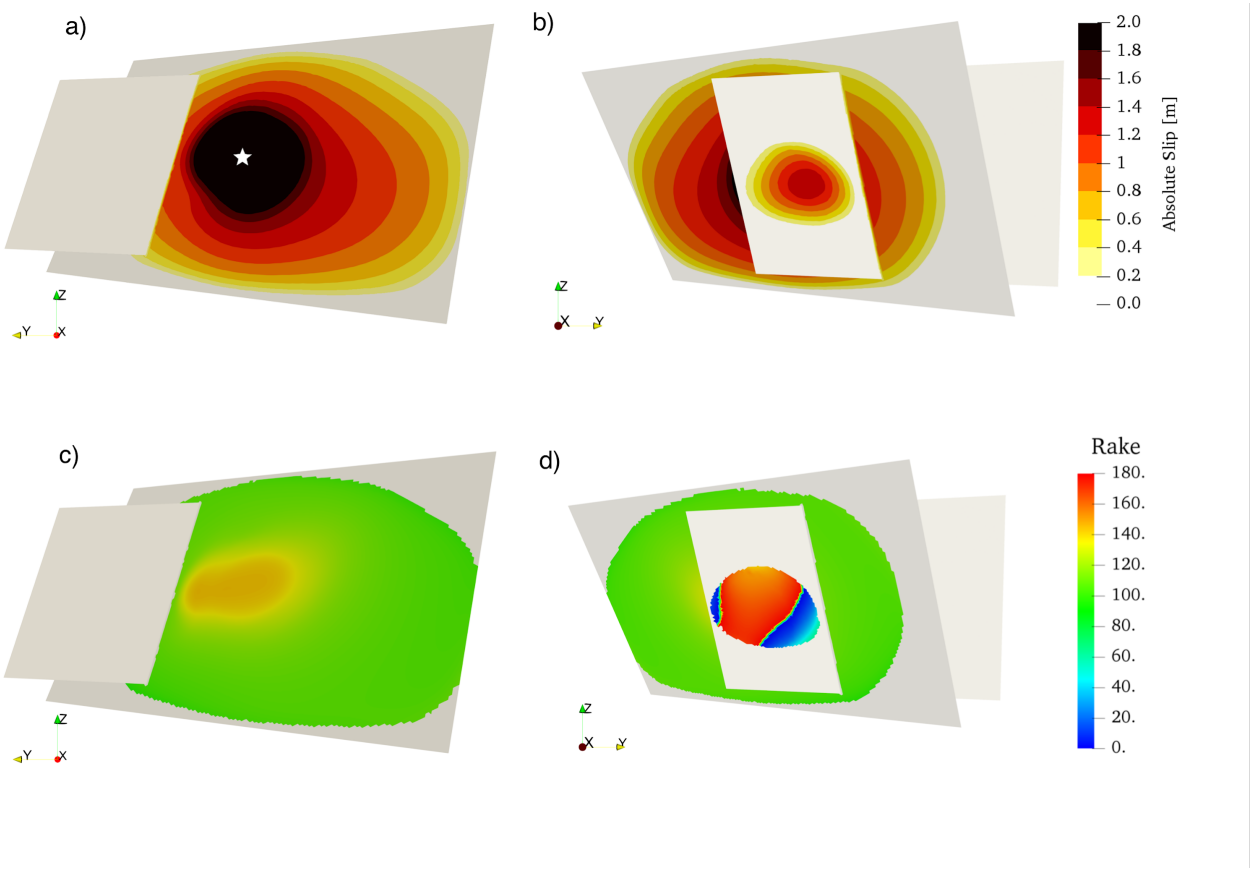

Figure 6. Distribution of absolute fault slip (in m) in a) and b), and rake angles (in degrees) in c) and d) for the preferred dynamic rupture scenario (Model 2F) a) and c) view from North highlighting the main fault rupture. b) and d) view from South highlighting the rupture of a portion of the secondary fault. The white star in panel a) marks the considered hypocenter location.

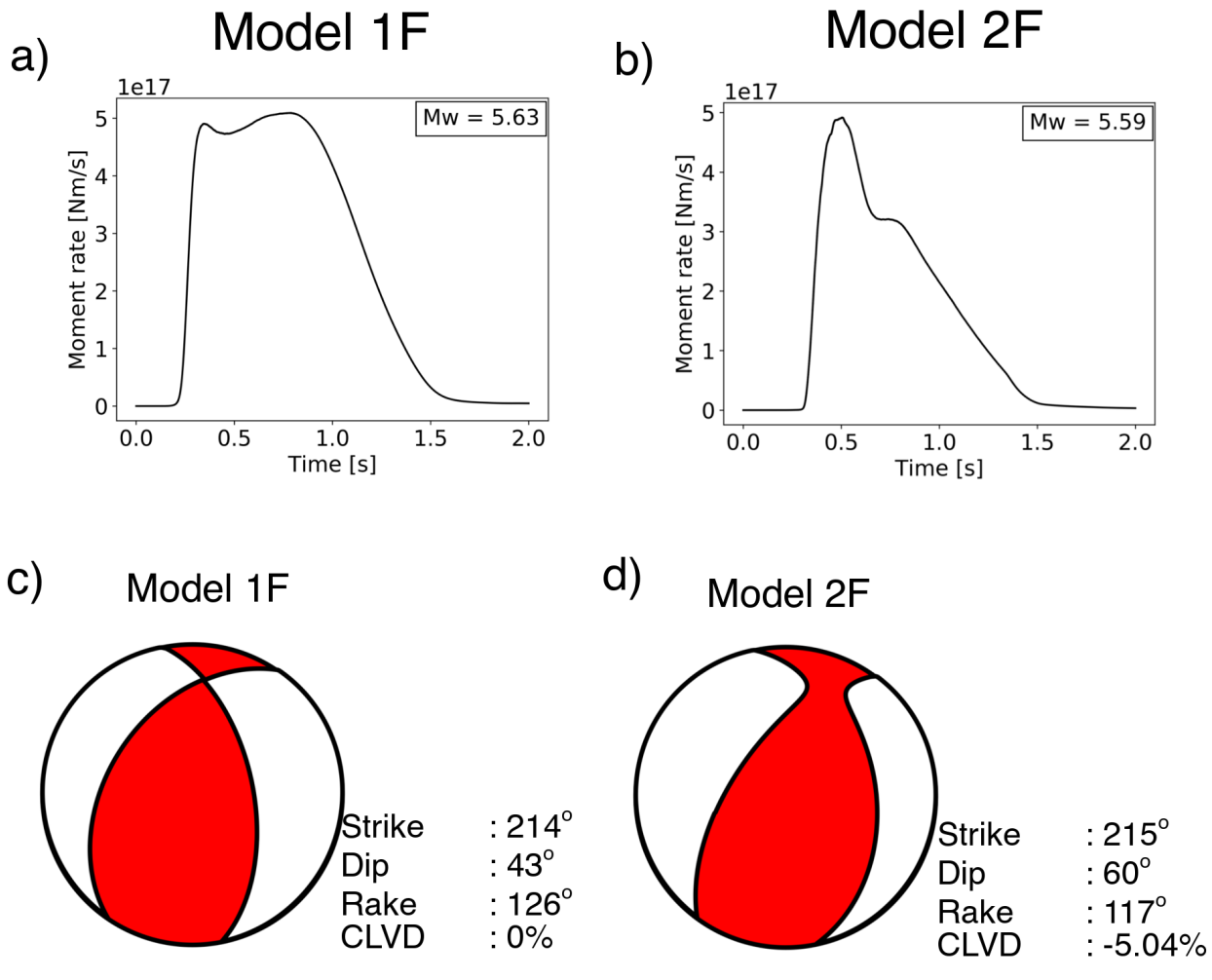

1167

1168 **Figure 7**. Moment rate release of a) Model 1F and b) Model 2F and moment tensor

1169 representation of the preferred one-fault c) and two-fault d) models.

1170

1171

1172

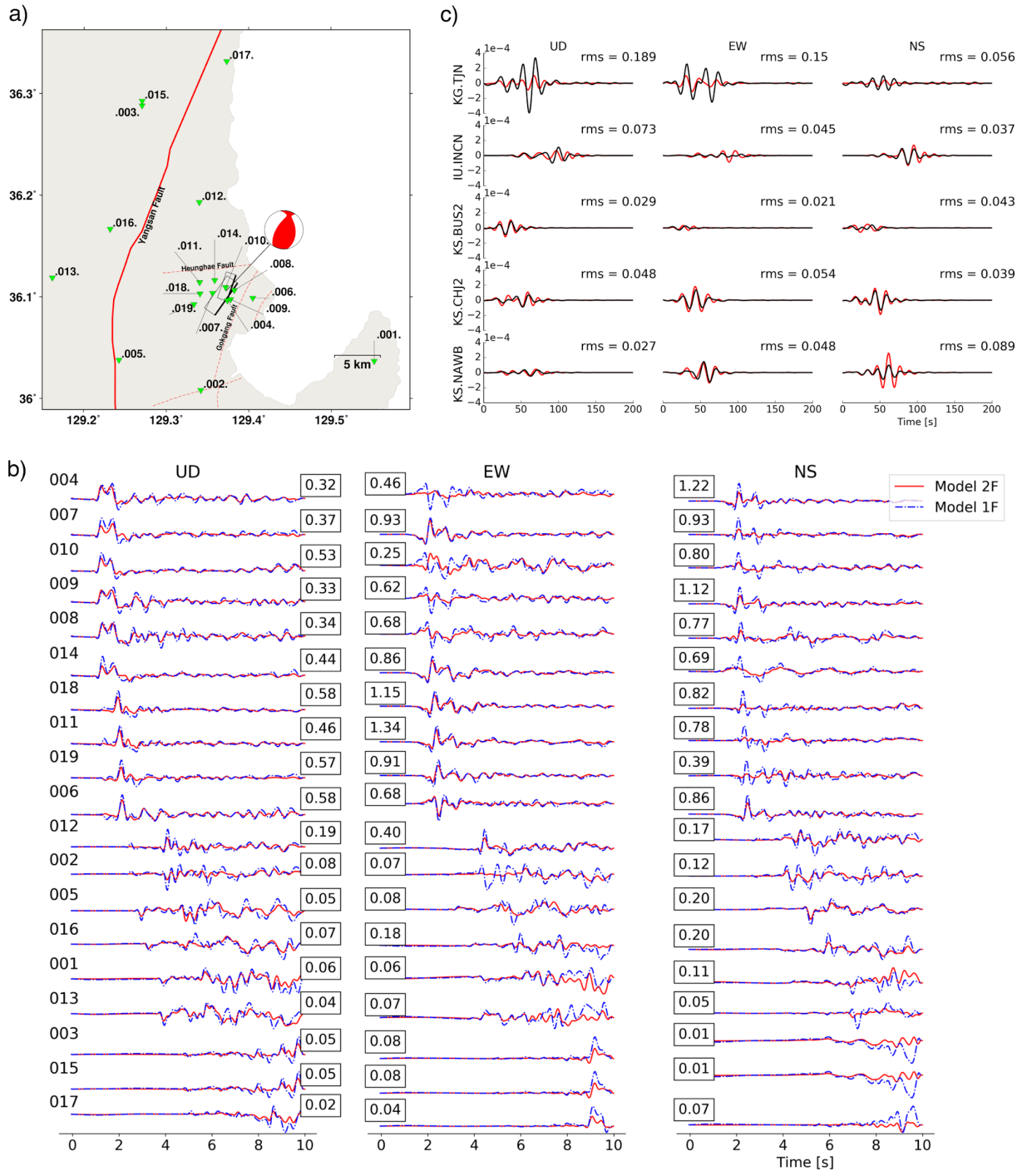

1173

1174 **Figure 8**. Comparison of synthetic and observed ground motion waveforms. a) Distribution of

1175 virtual stations (green triangles) at which synthetic waveforms are compared in b). The beachball

1176 is the moment tensor representation of the preferred 2 planes model scenario (Model 2F). Solid

and dashed red lines represent the mapped Yangsan fault surface trace and the interpreted fault traces near the Pohang EGS site, respectively. The two rectangles show the location and geometry of the faults used in this study. b) Comparison of synthetic waveforms using one (Model 1F, blue dashed lines) and two fault planes (Model 2F, red solid lines) at the 19 dummy stations located in a). A 0.1 - 2 Hz 4^{th} order Butterworth filter is applied to all traces. All traces are normalized. For each trace, the maximum velocity amplitude (in m/s) of Model 1F is indicated within a black square. c) Observed (black) and synthetic (red) waveforms for five regional stations for up-down (UD), east-west (EW) and north-south (NS) components (all located in South Korea, see blue triangles in Figure 1. t = 0 s denotes the origin time of the Pohang earthquake. A 0.033-0.08 Hz 4^{th} order Butterworth filter is applied to all traces. Synthetic regional waveforms are generated from the preferred dynamic rupture scenario Model 2F using Instaseis (Krischer et al., 2017) and 2 s accurate Green's functions based on the PREM anisotropic model.

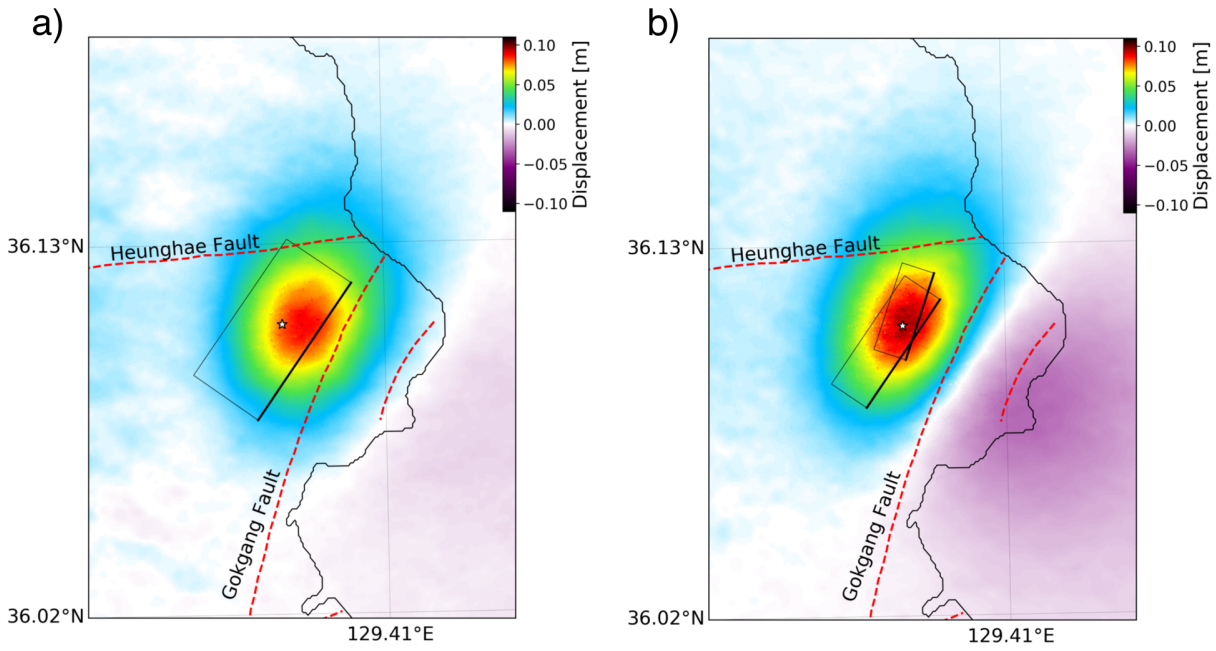

Figure 9. ((a) and (b)) Co-seismic surface displacements in the InSAR Line-of-sight (LoS) direction (in m) generated by a) Model 1F; one-plane (rectangle) and b) Model 2F; two-planes (two rectangles) preferred dynamic rupture scenario, respectively. The dashed red lines represent the traces of the interpreted faults near the EGS site.

APPENDIX

A1 Friction parameters

To parameterize the frictional behavior, we use laboratory-based rapid velocity weakening friction law proposed by the community benchmark problem TPV104 Southern California Earthquake Center (SCEC-benchmark) (Harris et al., 2018). The friction law is adapted from - the formulation introduced by Dunham et al. (2011a). The governing equations in our notation are described in Ulrich et al. (2019a), the implementation in SeisSol is described and verified in Pelties et al. (2014). Figure S1b shows the depth-dependent direct effect a and weakening slip velocity V_W. The evolution effect parameter b is set constant. We apply a velocity strengthening zone at the top 200 m of all faults to smoothly stop rupture. Within this zone, values for a and V_W increase linearly ranging from 0.01 and 0.1 m/s below depth of 3.3 km to 0.02 and 1.0 m/s to the surface, respectively. Table 1 lists all friction parameters used in this study.

Table 1. *Fault friction parameters assumed in this study*

Parameter	Symbol	Value
Direct effect parameter	a	0.01 - 0.02 z≤3.3 km and 0.01 z > 3.3 km

Evolution effect parameter	b	0.014
Reference slip velocity	V_0	10^{-6}m/s
Steady-state friction coefficient at V_0	f_0	0.6
State-evolution distance	L	0.2 m
Weakening slip velocity	V_W	0.1 - 1.0 z≤3.3 km and 0.1 z > 3.3 km
Fully weakened friction coefficient	f_W	0.1
Initial slip rate	V_{ini}	10^{-16}m/s

A2 Nucleation procedure

To nucleate the earthquake, we apply a time-dependent overstress centered at the hypocenter location, that is at longitude and latitude of 129.37° and 36.11°, respectively, and at a depth of 4.27 km. The time-dependent overstressed nucleation area $R_{nuc}(t)$ is determined by increasing the initial relative prestress ratio R_0 as:

$$R_{nuc}(t) = R_0 + \Omega(r) \times S(t) \quad \text{(A2.1)}$$

where $\Omega(r)$ is a Gaussian-step function, r is the radius from the hypocenter, and $S(t)$ denotes the smoothed step function. The Gaussian-step function is defined as:

$$\Omega(r) = \xi\, exp(\frac{r^2}{r^2 - {r_c}^2}) \quad \text{for r} < r_c\ ; \qquad \Omega(r) = 0 \quad \text{otherwise} \qquad \text{(A2.2)}$$

where ξ is the overstressed initial relative prestress ratio and $r_c = 500$m is the radius of the nucleation patch. We only overstress the main fault plane; In the nucleation region, we set ξ to 2, and apply an overstress characterized by S_{Hmax}= 77° and $v = 0.1$. These values are set by trial-and-error to allow rupture to propagate spontaneously with the least magnitude of overstress and to limit fault slip inside the nucleation patch. The orientation of S_{Hmax} is also in accordance with Korean Government Commission, 2019 and Ellsworth et al. (2019) which suggest optimally oriented stress orientation and critically stressed inside the nucleation zone. The smoothed step function is formulated as:

$$S(t) = exp(\frac{(t-T)^2}{t \times (t - 2 \times T)}) \quad \text{for } 0 < t < T;\ S(t) = 1 \quad \text{for } t \geq T \qquad \text{(A2.3)}$$

where $T = 0.4$s is the nucleation time.

A3 Methodology

A3.1 Numerical method

We use the open-source software SeisSol (Dumbser and Käser, 2006; Pelties et al., 2014; Uphoff et al., 2017; Wollherr et al., 2018) (https://github.com/SeisSol/SeisSol), which couples seismic wave propagation in complex media and frictional fault failure. SeisSol uses an Arbitrary high-order DERivative-Discontinuous Galerkin (ADER-DG) approach which achieves high-order accuracy in space and time (Käser and Dumbser, 2006). SeisSol uses flexible non-uniform

1243 unstructured tetrahedral mesh, which allows accounting for complex geometric features such as
1244 3D fault networks or high-resolution topography across a large range of scales: from small-scale
1245 fault roughness, large-scale fault structures to fault-to-fault interaction. Dynamic rupture
1246 simulations are sensitive to geometrically complexity of faults (Dunham et al., 2011b; Shi and
1247 Day, 2013; Uphoff et al., 2017; Wollherr et al., 2018, 2019; Ulrich et al., 2019a, 2019b).

1248 A high resolution and accurate simulation are essential to resolve the detailed processes of
1249 rupture propagation of the intersected fault geometry. We motivate the presented deterministic
1250 parameter study with the computational feasibility of many such simulations. While the feasibility
1251 of dynamic rupture inversion and statistical learning approaches has been demonstrated (e.g.
1252 Peyrat et al. 2001; Bauer et al., 2018, Happ et al. 2019, Gallovič et al. 2019a, Gallovič et al. 2019b),
1253 these are restricted by near-field data availability and the computational cost of each forward
1254 dynamic rupture model.

1255 SeisSol is verified in a wide range of benchmark problems, including dipping faults,
1256 branched and curved faults, on-fault heterogeneity, and laboratory-based friction laws (de la
1257 Puente et al., 2009; Pelties et al., 2012; Pelties et al., 2014; Wollherr et al., 2018,) in line with the
1258 SCEC-Benchmark Dynamic Rupture code verification exercises (Harris et al., 2011; Harris et al.,
1259 2018) as well as against analytical reference solutions for seismic wave propagation (e.g., Uphoff
1260 and Bader, 2016; Wolf et al., 2020). Fast time to solution is achieved thanks to end-to-end
1261 optimization (Breuer et al., 2014; Heinecke et al., 2014; Rettenberger et al., 2016), including an
1262 efficient local time-stepping algorithm (Breuer et al., 2016, Uphoff et al., 2017). This efficient
1263 algorithm on high-performance computing architecture provides up to ten-fold speed up (Uphoff
1264 et al., 2017).

SeisSol allows accounting for off-fault yielding. Inelastic energy dissipation influences rupture dynamics such as rupture speed and rupture style (e.g., Gabriel et al., 2013). Off-fault plasticity is incorporated using the off-line code generator to compute matrix operations in an efficient way (Wollherr et al., 2018). SeisSol also supports visco-elastic rheologies, using an off-line code generator similar to that off-fault plasticity. In this study, we use a spatiotemporal discretization of polynomial degree $p = 4$ ($O5$) for all simulations.

A3.2 Mesh generation

The simulation domain and fault plane geometry model are created using third-party software GoCad (Emerson paradigm holding, 2018) in a Cartesian coordinate system. We discretize the unstructured tetrahedral mesh using the meshing software Simmodeler (Simmetrix Inc., 2017). The mesh element edge length size to 50 m close to the fault plane and 200 m at the surface topography, yielding a 4 million volume cell mesh. The mesh size on the fault plane is examined prior to the simulation by calculating the cohesive zone (or process zone) to ensure convergence. Wollherr et al. (2018, 2019) provide a way to resolve the cohesive zone for the case of SeisSol. To save the computational costs and at the same time avoid reflection from the domain boundary, we gradually increase the edge length size of the tetrahedral element by a factor of 6% away from the fault plane and surface topography. Figure 3 depicts the unstructured tetrahedral mesh used in this study, overlain by a snapshot of the absolute velocity field at simulation time 5 s, for our preferred dynamic rupture model (Model 2F), highlighting the effect of the topography on the near-field ground motions.

The locally refined mesh and high-order spatiotemporal discretization allow capturing the high-frequency content of the waveforms with high accuracy (little numerical dispersion), especially in the near-fault region. We estimate the maximum resolved frequency is up to 4 Hz

within 7 km distance from the fault zone, and around 1 Hz at 30 km distance from the fault. Simulating 5 s typically requires 15 minutes (average run-time) on Intel Haswell cores with 128 nodes using supercomputer Cray XC40 Shaheen-II, King Abdullah University of Science and Technology, Saudi Arabia.

Electronic supplement to

Dynamic fault interaction during a fluid-injection induced earthquake: The 2017 Mw 5.5 Pohang event

By K. H. Palgunadi, A.-A Gabriel, T. Ulrich, J. A. Lopéz-Comino, P. M. Mai

---

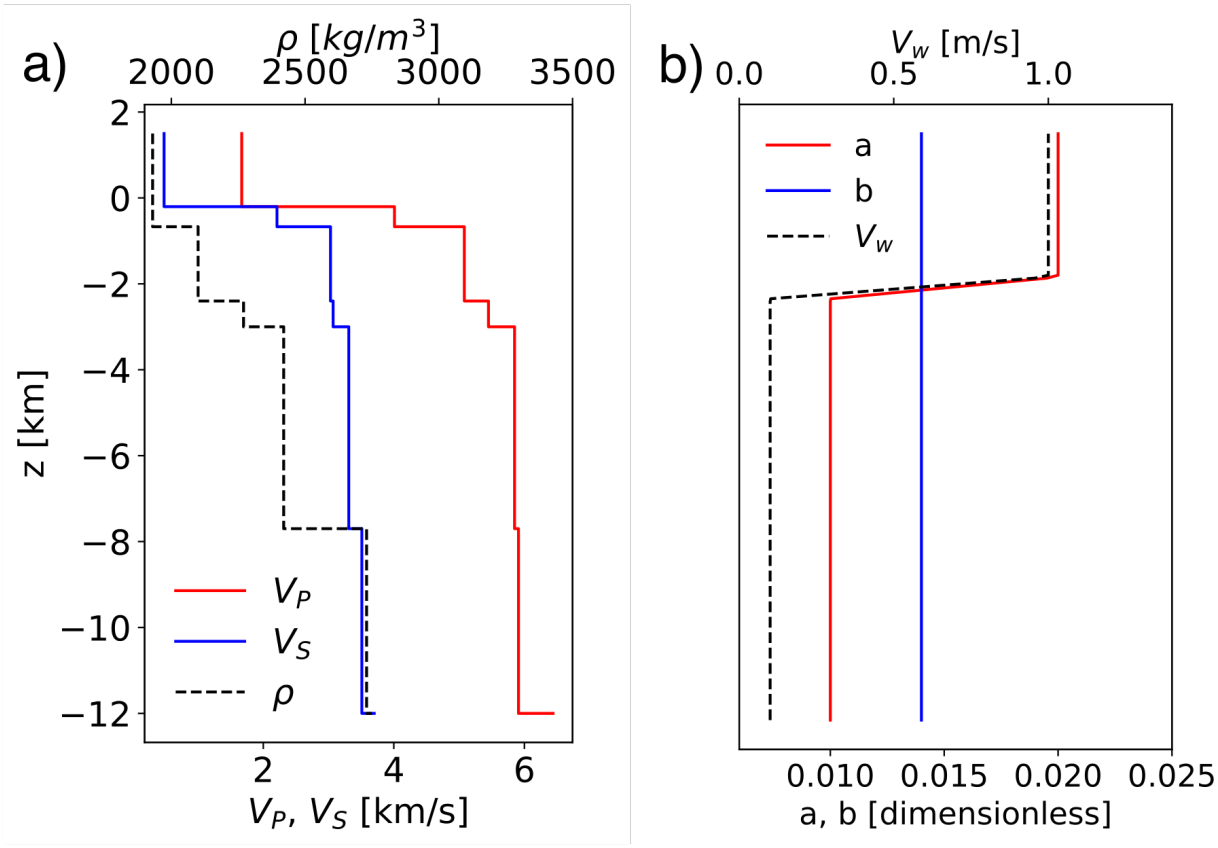

Figure S1. Vertical profiles of a) the 1-D model of seismic wave speeds by Woo et al. (2019) and by Korean Government Commission (2019). Panel b) displays the depth-dependent parameters of the velocity weakening rate-and-state friction law.

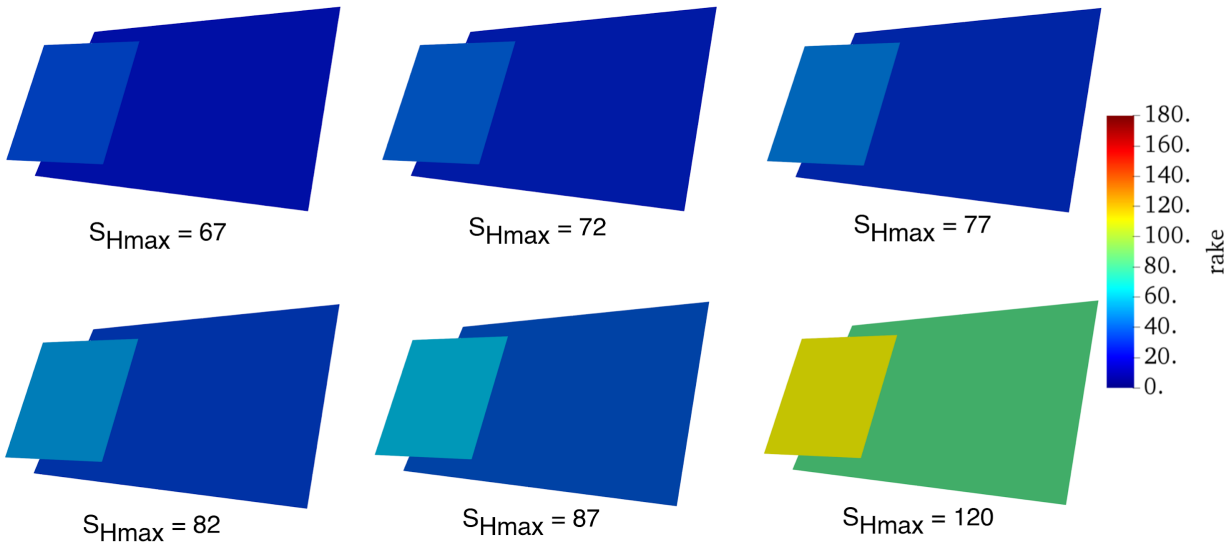

1304

1305 **Figure S2**. Rake of initial (at t=0) shear traction for exemplary orientations of maximum horizontal

1306 stress S_{Hmax} (see also Table S1). Thrust-faulting is favoured for S_{Hmax}=120°. Note that

1307 S_{Hmax}=77° corresponds to the findings of Ellsworth et al. (2019).

1308

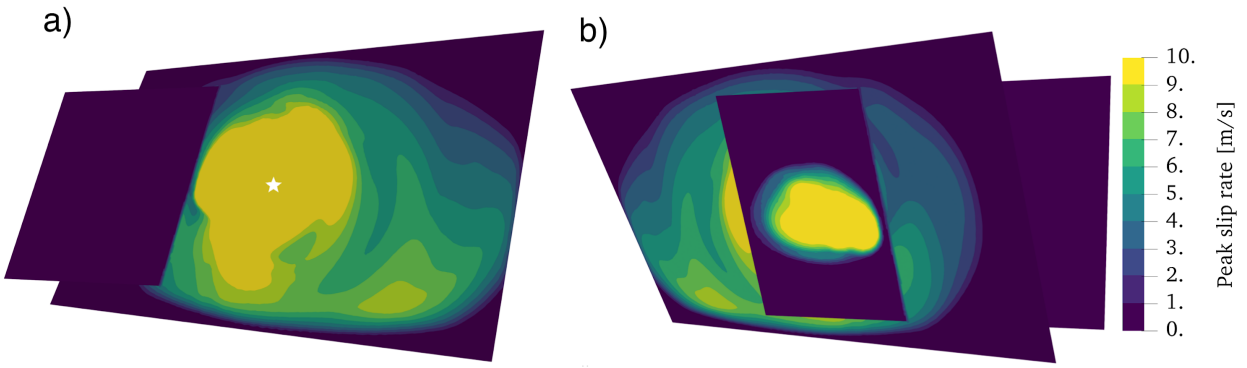

1309

1310 **Figure S3**. Peak slip-rate of the Model 2F. The maximum peak slip rate (saturated yellow color)

1311 outside the nucleation zone is 15 m/s. View from a) North and b) South.

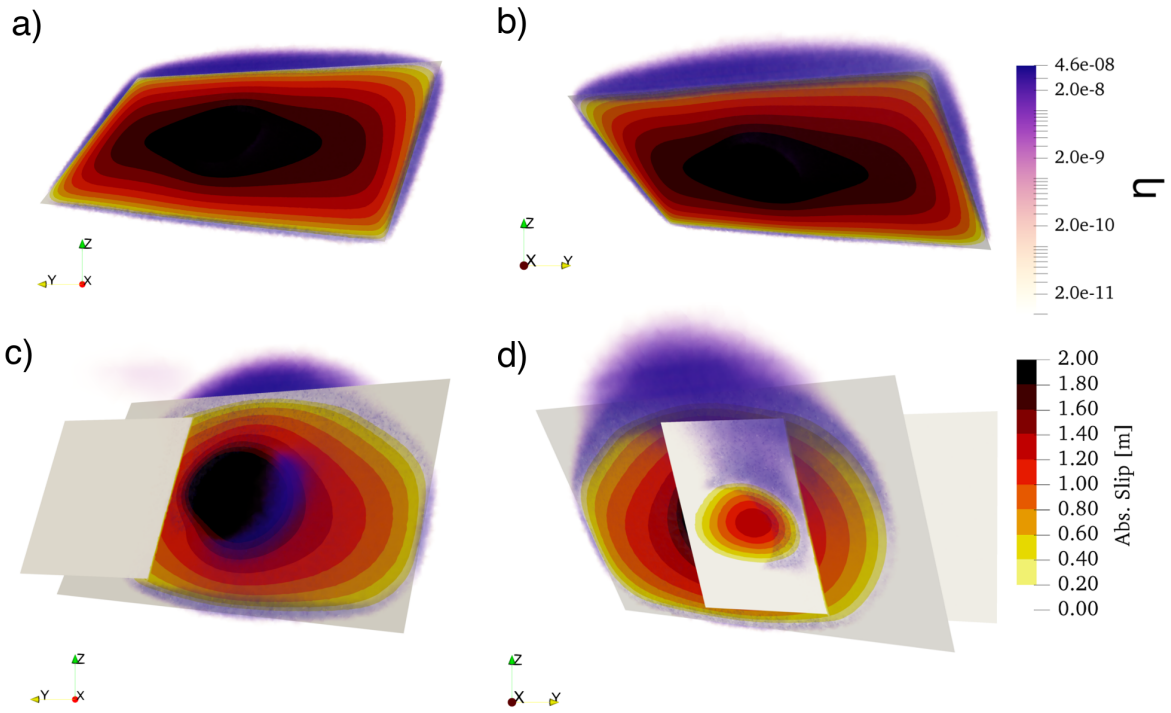

Figure S4. Asymmetric off-fault plastic deformation for Model 1F (a and b) and for Model 2F (c and d). a) and c) view from North b) and d) view from South. The accumulated volumetric plastic strain is mapped into the scalar quantity ηas noted by the purple colorbar.

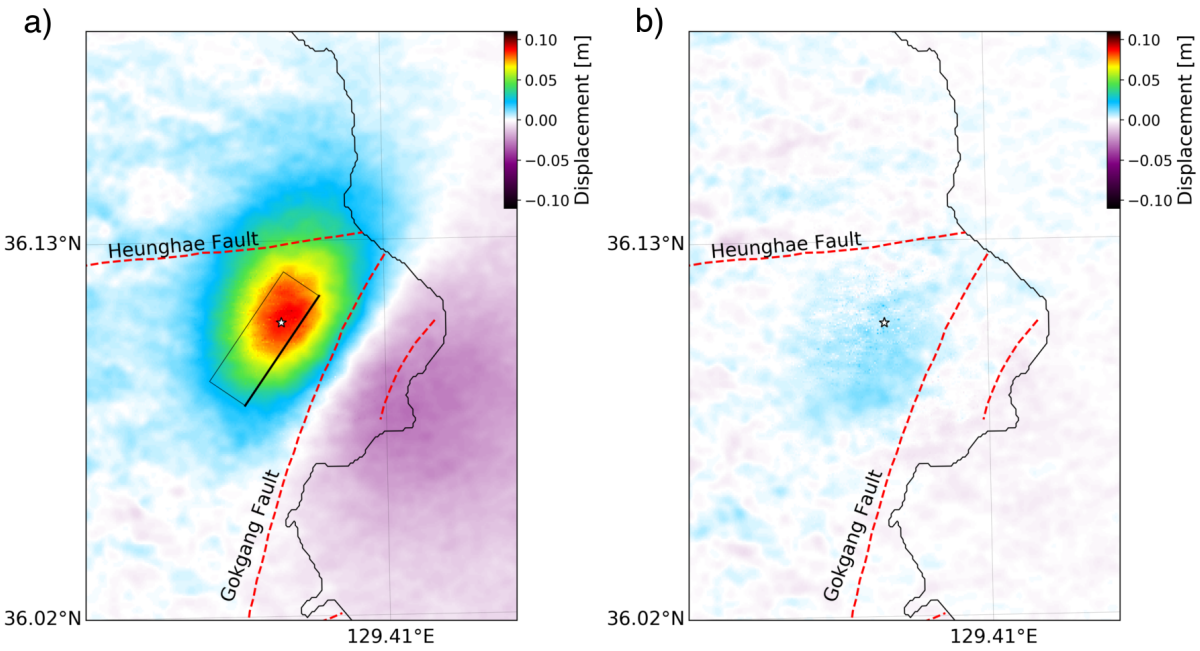

Figure S5. Surface displacements. a) Co-seismic surface displacements using only the main fault plane of Model 2F. Rectangle illustrates the fault plane. b) Residual of Model 2F with respect to Model 2F by using only the main fault plane. The dashed red lines represent the traces of the interpreted faults near the EGS site. The white star represents the epicenter of the Pohang earthquake.

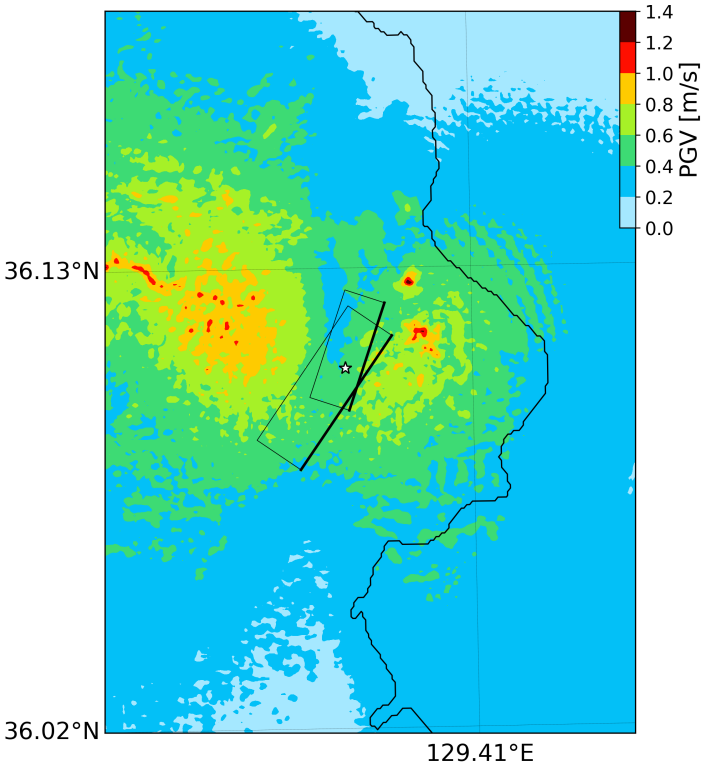

Figure S6. Peak ground velocity shake-map (in m/s, based on GMRotD50 (Boore et al., 2006)) for preferred scenario Model 2F, color-contoured 0.2 increments. The white star denotes the epicenter of the Pohang earthquake.

Table S1. Rake of initial shear traction on the faults of Model 2F

S_{Hmax}	Main fault rake (°)	Secondary fault rake (°)
52	0	12
57	3	16
62	7	20
67	11	24
72	15	29
77	19	35
82	23	41

87	28	48
92	34	57
97	40	66
102	47	77
107	55	88
112	64	100
120	80	110
125	91	130
130	110	140
135	115	130
140	120	150

Movie M1: Slip-rate of Model 2F.

(link: https://drive.google.com/open?id=1nm3HZ_YOD-j8t_YatTFfs9prVKplEExj)

Reference:

Boore, D. M., J. Watson-Lamprey, and N. A. Abrahamson, 2006, Orientation-Independent Measures of Ground Motion, Bull. Seismol. Soc. Am., 96, no. 4A, 1502–1511, doi: 10.1785/0120050209.